Ripple Transport in Helical-Axis Advanced Stellarators — A Comparison With Classical Stellarator/Torsatrons

C.D. Beidler, W.N.G. Hitchon

IPP 2/307 August 1993

MAX-PLANCK-INSTITUT FÜR PLASMAPHYSIK

85748 GARCHING BEI MÜNCHEN

MAX-PLANCK-INSTITUT FÜR PLASMAPHYSIK

GARCHING BEI MÜNCHEN

Ripple Transport in Helical-Axis Advanced Stellarators — A Comparison With Classical Stellarator/Torsatrons

C.D. Beidler, W.N.G. Hitchon

IPP 2/307 August 1993

Die nachstehende Arbeit wurde im Rahmen des Vertrages zwischen dem Max-Planck-Institut für Plasmaphysik und der Europäischen Atomgemeinschaft über die Zusammenarbeit auf dem Gebiet der Plasmaphysik durchgeführt.

RIPPLE TRANSPORT IN HELICAL-AXIS ADVANCED STELLARATORS — A COMPARISON WITH CLASSICAL STELLARATOR/TORSATRONS

C.D. Beidler
Max-Planck-Institut für Plasmaphysik
IPP–EURATOM Association
D-85748 Garching bei München, Germany

W.N.G. Hitchon
University of Wisconsin-Madison
Department of Electrical and Computer Engineering
Madison, WI 53706, USA

ABSTRACT

Calculations of the neoclassical transport rates due to particles trapped in the helical ripples of a stellarator's magnetic field are carried out, based on solutions of the bounce-averaged kinetic equation. These calculations employ a model for the magnetic field strength, B, which is an accurate approximation to the actual B for a wide variety of stellarator-type devices, among which are Helical-Axis Advanced Stellarators (Helias) as well as conventional stellarators and torsatrons. Comparisons are carried out in which it is shown that the Helias concept leads to significant reductions in neoclassical transport rates throughout the entire long-mean-free-path regime, with the reduction being particularly dramatic in the ν^{-1} regime. These findings are confirmed by numerical simulations. Further, it is shown that the behavior of deeply trapped particles in Helias can be fundamentally different from that in classical stellarator/torsatrons; as a consequence, the beneficial effects of a radial electric field on the transport make themselves felt at lower collision frequency than is usual.

I. INTRODUCTION

As a refinement and further development of the original Advanced Stellarator concept [1], the Helical-Axis Advanced Stellarator (Helias) [2] has been formulated as a means of greatly reducing the Pfirsch-Schlüter equilibrium current which flows in a stellarator plasma while also maintaining a global magnetic well. This combination allows finite-pressure configurations with average beta, $\langle\beta\rangle \geq 5\%$, with minimal Shafranov shift of the plasma column and only small changes in the vacuum rotational transform and shear profiles [3]. That these favorable characteristics may simultaneously exist for real magnetic fields has been demonstrated using an optimization procedure based on the observation that the shape of the outermost magnetic surface completely determines the properties of the confinement region [2,4] (thus allowing the solution of boundary value problems during optimization, with parameters describing the shape of the last magnetic surface serving as the optimization variables). In a subsequent step, the desired magnetic field is realized using a finite number of discrete current-carrying non-planar coils [5-6]. Taken together, the advantageous physical properties of the magnetic field and the ability to realize such a field through the use of modular coils makes the Helias concept particularly favorable for future stellarator development; these points weighed heavily in the decision to base the design of the future large stellarator Wendelstein 7-X [7] on the Helias concept.

Along with their desirable MHD properties, Helias configurations have favorable neoclassical transport characteristics as well, both in the collisional (plateau) and collisionless (long-mean-free-path) regimes. In the plateau regime, the reduction of the Pfirsch-Schlüter current leads to a neoclassical particle flux, Γ, which is less than that of an axisymmetric device of equal aspect ratio and rotational transform [8]. The amount of reduction depends on the particular Helias configuration, but typically the ratio $\Gamma_{Helias}/\Gamma_{axisym}$ lies between 1/6 and 1/2. On the other hand, classical stellarator/torsatron devices strictly satisfy $\Gamma_{stel}/\Gamma_{axisym} > 1$ [9].

The transport characteristics of the various Helias configurations are more difficult to quantify in the long-mean-free-path (*lmfp*) regime. In this case the detailed structure of the magnetic field plays a crucial role with particles trapped in local *helical-ripple* wells giving rise to the dominant transport mechanism. It has been pointed out that some Helias fields have a small variation of the minimum value of B along a field line [8] and hence are similar to so-called "drift-optimized" stellarator fields [10-13]. Other Helias fields are "quasi-helical" [4], i.e. in magnetic coordinates their harmonic structure approximates that of a straight cylindrical stellarator. In this latter case the magnitude of the toroidal modulation of B is much less than the inverse aspect ratio, ϵ_t, and hence the radial drift of particles away from magnetic surfaces is reduced. One would expect

in both of the above cases that neoclassical transport losses in the *lmfp* regime should be reduced. Monte Carlo simulations have also been carried out for several Helias configurations with encouraging results [14,15].

What has been lacking thus far, however, is a detailed analytical examination of the neoclassical transport characteristics of Helias in the *lmfp* regime. Such an analysis has been complicated previously by the limitations of the existing analytic theory; these arise principally because (i) the simple, one-helical-harmonic magnetic field models which have most often been assumed do not provide an adequate description of a Helias field, and (ii) a single theory capable of handling the entire range of low collision frequencies did not exist. Both of these shortcomings have been largely overcome by the advent of a power-series solution of the bounce-averaged kinetic equation which is valid for all collision frequencies characteristic of the long-mean-free-path regime [16]. The extension of this solution to deal with a more general model magnetic field — one which provides an equally accurate representation of B for Helias configurations and conventional stellarators and torsatrons — is one of the principal topics of this paper and is described in Section III.

To further aid in clarifying the favorable transport characteristics of the Helias, the bounce-averaged kinetic equation will also be solved in the ν^{-1} regime (the more collisional end of the *lmfp* regime where the transport coefficients scale inversely with collision frequency) by means of the more conventional asymptotic analysis. This solution is presented in Section IV. The result is instructive because it explicitly shows the dependence of the neoclassical transport coefficients in this regime on the interplay of various magnetic-field quantities and because it allows a direct comparison with the more general results obtained in Section III.

All results are derived in a general form, greatly facilitating a comparison of specific Helias configurations with other stellarator-type devices. This comparison is carried out in Sections IV and V. Also presented in Section V are numerical results obtained by application of the well-known Monte Carlo simulation technique; these provide independent confirmation of neoclassical transport coefficients obtained analytically. Discussion of the results and concluding remarks are given in Section VI.

II. THE MODEL MAGNETIC FIELD

Before proceeding to these topics, however, some general comments are in order, especially with respect to the model magnetic field which will be used. Throughout this work, the magnetic coordinate system (r, ϕ, θ) [17] will be employed; here r is a flux surface label, related to the toroidal flux through the expression $\psi = B_0 r^2/2$, and ϕ,θ

are toroidal and poloidal angle-like variables, respectively. In this coordinate system, a sufficiently general expression for the magnitude of the magnetic field is given by

$$\frac{B}{B_0} = \sum_{m,\ell} C_{m,\ell}(r) \cos mp\phi \cos \ell\theta + \sum_{m,\ell} S_{m,\ell}(r) \sin mp\phi \sin \ell\theta, \qquad (1)$$

where p is the field period number.

An accurate representation of any real stellarator/torsatron field typically requires that a large number of terms in the expansions be kept. This is especially true in Helias configurations for which the magnetic field is produced by a large number of discrete non-planar coils (typically 10 per field period); high-order m harmonics are present in a Helias field which would be absent for a continuously wound stellarator. Indeed, the decomposition of a Helias magnetic field according to Equation (1) invariably yields more than 50 contributing harmonics. The great majority of these harmonics are very small in magnitude, however, and one finds that a good approximation to B for both Helias and conventional stellarator-type devices is obtained if the expansion is limited to include only $m = 0$ and $m = 1$ terms. Given this simplification, it is possible to construct the model magnetic field

$$B/B_0 = C_{0,0} - |C_{0,1}| \cos\theta + C_{0,2} \cos 2\theta - \epsilon_H(r,\theta) \cos(\chi - p\phi)\,, \qquad (2)$$

where the $m = 1$ harmonics are identified with the stellarator's helical ripple

$$\epsilon_H(r,\theta) = \epsilon_h(r)\big(1 - \sigma_1(r)\cos\theta - \sigma_2(r)\cos 2\theta\big),$$

the phase angle χ is determined from

$$-\cos\chi = \mathbf{C}/\epsilon_H\,, \qquad -\sin\chi = \mathbf{S}/\epsilon_H\,,$$

and where the geometric quantities are given by

$$\mathbf{C} = C_{1,0} + C_{1,1}\cos\theta + \cdots + C_{1,\ell}\cos\ell\theta,$$

$$\mathbf{S} = S_{1,1}\sin\theta + \cdots + S_{1,\ell}\sin\ell\theta,$$

$$\epsilon_h = \frac{1}{2\pi}\int_0^{2\pi} d\theta(\mathbf{C}^2 + \mathbf{S}^2)^{1/2}\,,$$

$$\sigma_1 = -\frac{1}{\pi\epsilon_h}\int_0^{2\pi} d\theta(\mathbf{C}^2 + \mathbf{S}^2)^{1/2}\cos\theta\,,$$

$$\sigma_2 = -\frac{1}{\pi\epsilon_h}\int_0^{2\pi} d\theta(\mathbf{C}^2 + \mathbf{S}^2)^{1/2}\cos 2\theta\,.$$

To illustrate the relative magnitudes of the harmonics which are incorporated into this model magnetic field and those which are neglected, it is instructive to look at the general decomposition of B for several realistic magnetic fields. This is done in Figure 1 for the Helias HS5V10N (the reference configuration for Wendelstein 7-X), for the Large Helical Device (LHD) heliotron/torsatron [18], for the classical stellarator Wendelstein VII-A (W VII-A) [19] and for the URAGAN-2M (U2M) torsatron [20]. In each case all harmonics which attain a magnitude of at least $0.05\epsilon_h(r)$ are shown. For LHD and W VII-A there are no harmonics with $m > 1$ which reach this threshold; for LHD the largest of such harmonics has been plotted to indicate their magnitudes while for W VII-A, harmonics with $m > 1$ are truly so small that they cannot be discerned on the figure. The $m = 4$ terms in the U2M spectrum are a consequence of the toroidal field coil set (4 coils per field period) which provides a significant portion of this device's magnetic field. Discrete-coil ripple of this type is also present for HS5V10N, however the large number of modular coils per field period envisioned for the device (10 in this case) ensures that harmonics associated with this "modular" ripple lie well below the $0.05\epsilon_h(r)$ threshold except for the outermost flux surfaces. The effect such harmonics have on the neoclassical transport characteristics of the device is thus small [21] and will be ignored throughout the rest of this work.

The smallness of the neglected harmonics is not the only measure of the accuracy of the model field given in Equation (2), of course, since there is no guarantee *a priori* that higher-order terms neglected in the formulation of ϵ_H (e.g. $\sigma_3 \cos 3\theta$, $\sigma_4 \cos 4\theta$) are not essential to an accurate representation of the helical ripple. That these higher-order terms may indeed be neglected is illustrated in the frames of Figure 2, where the variation of B along a field line obtained from the general expression of Equation (1) is compared with the simplified model field of Equation (2). In the upper frame of each figure pair only harmonics with $m \leq 1$ have been considered, while in the lower frame the general expression for B/B_0 also includes all the remaining harmonics depicted in Figure 1. In the former case the agreement between the two curves is uniformly excellent; the additional harmonics present in the lower frames introduce small, although noticeable, discrepancies. In light of the usual approximations made in developing a tractable analytic theory, these discrepancies appear acceptable. This assertion, however, remains to be demonstrated.

The accuracy of the model field demonstrated in Figure 2 is of considerable importance since this field — unlike the general expression of Equation (1) — may be treated within the framework of bounce-averaged transport theory as described in the following section; although solutions of the bounce-averaged kinetic equation have been obtained for more general magnetic fields in the ν^{-1} regime [11-13], it is the model field of Equation (2) which makes it ultimately possible to derive a solution which is

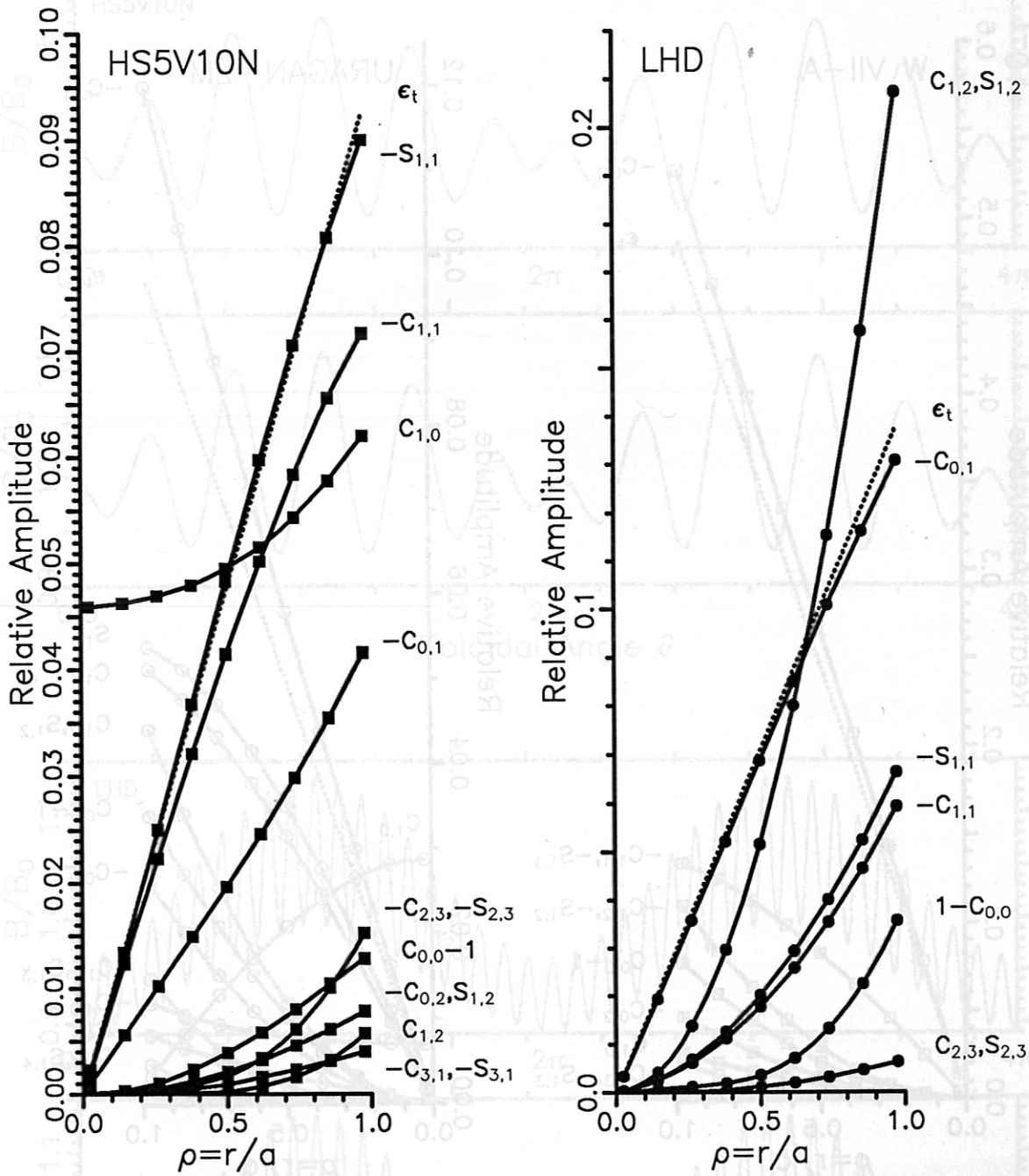

Figure 1. Magnetic-field-strength harmonics according to the decomposition given in Equation (1) are shown as a function of normalized plasma minor radius for the Helias HS5V10N, the torsatron LHD, the stellarator Wendelstein VII-A and the torsatron URAGAN-2M. Harmonics which attain a magnitude of at least $0.05\epsilon_h(r)$ *for at least*

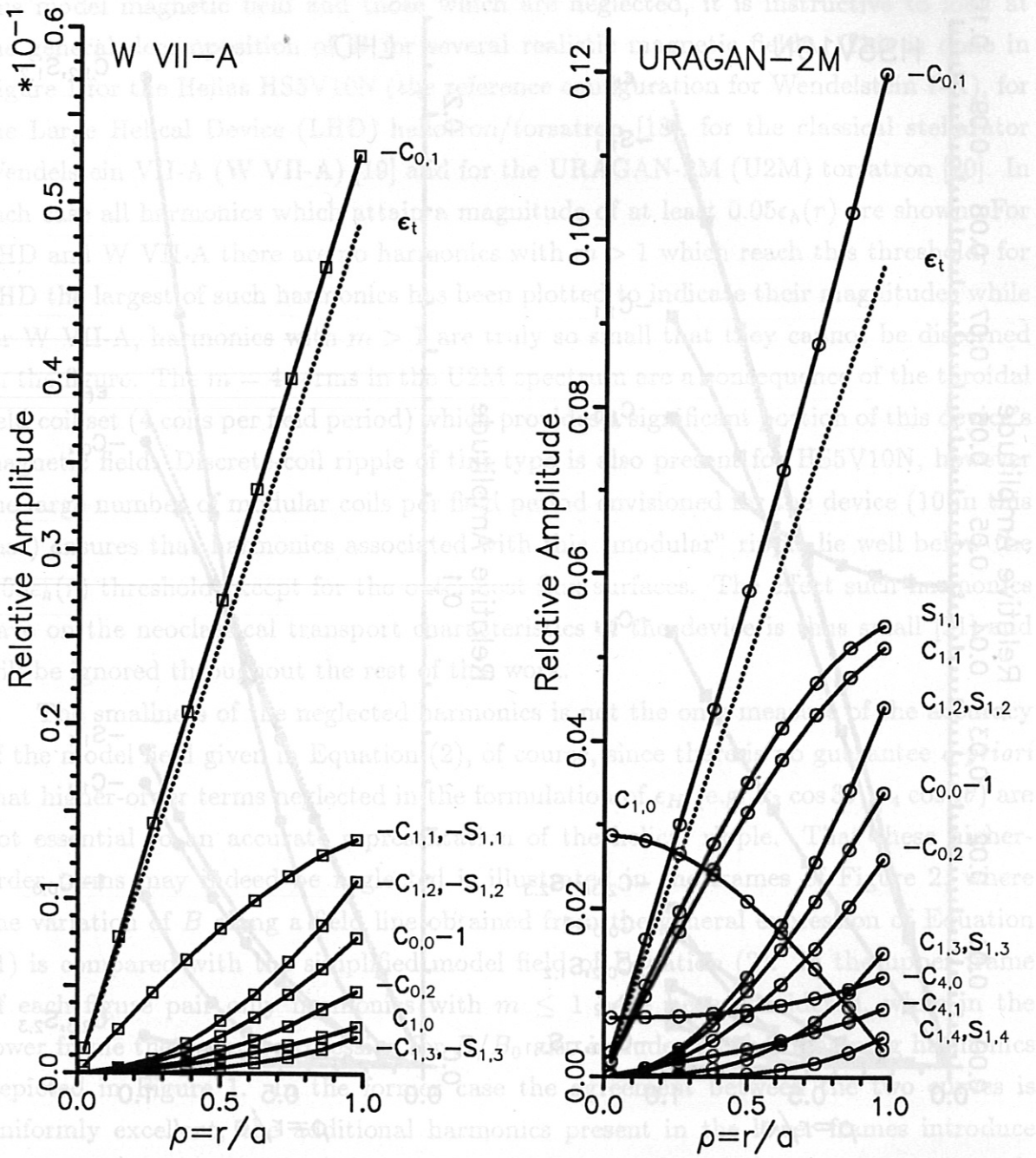

one value of r have been chosen (for LHD, the largest harmonic with $m > 1$ has also been plotted to indicate the magnitude of such harmonics). The inverse aspect ratio, $\epsilon_t \equiv r/R_0$, is shown for each configuration by the dotted line.

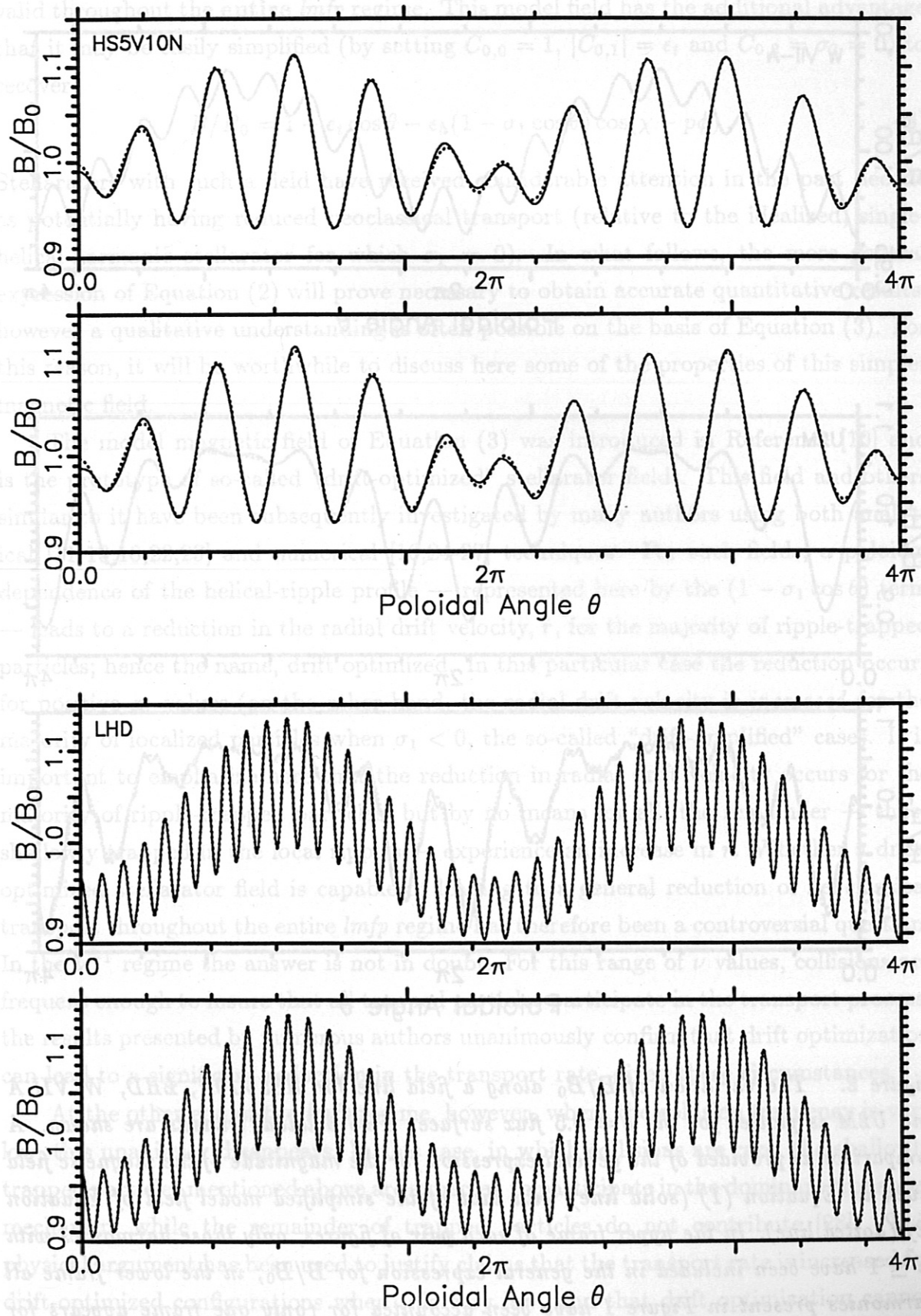
HS5V10N
B/B0
1.1
1.0
0.9
0.0
2π
4π
Poloidal Angle θ
LHD
B/B0
1.1
1.0
0.9
0.0
2π
4π
Poloidal Angle θ

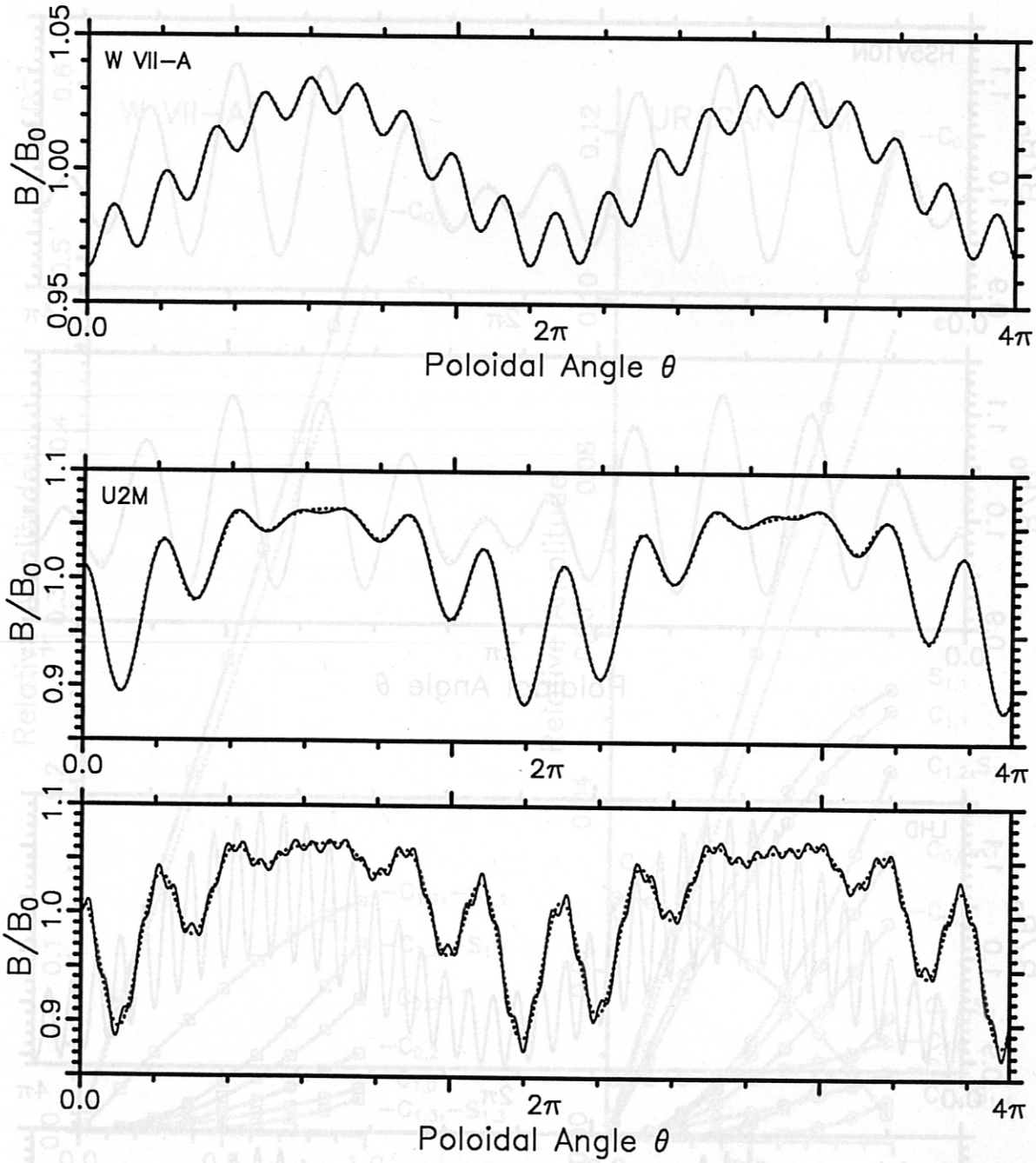

Figure 2. The variation of B/B_0 along a field line for HS5V10N, LHD, W VII-A and U2M is plotted for the $\rho = 0.5$ flux surface. Two poloidal transits are shown. A comparison is provided of the general expression for the magnitude of the magnetic field given in Equation (1) (solid line) with that of the simplified model field of Equation (2) (dotted line). In the upper frame of each pair of figures, only those harmonics with $m \leq 1$ have been included in the general expression for B/B_0; in the lower frame all harmonics present in Figure 1 have been accounted for (only one frame appears for W VII-A since this device has no harmonics with $m > 1$). The model field is the same in both frames of each figure pair.

valid throughout the **entire** *lmfp* regime. This model field has the additional advantage that it may be easily simplified (by setting $C_{0,0} = 1$, $|C_{0,1}| = \epsilon_t$ and $C_{0,2} = \sigma_2 = 0$) to recover

$$B/B_0 = 1 - \epsilon_t \cos\theta - \epsilon_h(1 - \sigma_1 \cos\theta)\cos(\chi - p\phi)\,. \tag{3}$$

Stellarators with such a field have received considerable attention in the past decade as potentially having reduced neoclassical transport (relative to the idealized, single-helical-harmonic stellarator for which $\sigma_1 = 0$). In what follows, the more general expression of Equation (2) will prove necessary to obtain accurate quantitative results, however a qualitative understanding is often possible on the basis of Equation (3). For this reason, it will be worthwhile to discuss here some of the properties of this simpler magnetic field.

The model magnetic field of Equation (3) was introduced in Reference [10] and is the prototype of so-called "drift-optimized" stellarator fields. This field and others similar to it have been subsequently investigated by many authors using both analytical [11-13,16,22,23] and numerical [16,24-27] techniques. For such fields, a poloidal dependence of the helical-ripple profile — represented here by the $(1 - \sigma_1 \cos\theta)$ term — leads to a reduction in the radial drift velocity, $\dot{r}$, for the majority of ripple-trapped particles; hence the name, drift optimized. In this particular case the reduction occurs for positive σ_1 values (on the other hand, the radial drift velocity is *increased* for the majority of localized particles when $\sigma_1 < 0$, the so-called "drift-amplified" case). It is important to emphasize here that the reduction in radial drift velocity occurs for the majority of ripple-trapped particles, but by no means for all; the remainder — those shallowly trapped in the local ripples — experience an increase in $\dot{r}$. Whether a drift-optimized stellarator field is capable of leading to a general reduction of neoclassical transport throughout the entire *lmfp* regime has therefore been a controversial question. In the ν^{-1} regime the answer is not in doubt. For this range of ν values, collisions are frequent enough to insure that all trapped particles participate in the transport process; the results presented by numerous authors unanimously confirm that drift optimization can lead to a significant reduction in the transport rate, given these circumstances.

At the other end of the *lmfp* regime, however, where the collision frequency is very low, this unanimity disappears. In this case, in which collisions are rare, the shallowly trapped particles mentioned above are expected to participate in the dominant transport mechanism while the remainder of trapped particles do not contribute [28]. This physical argument has been used to justify claims that the transport rate is increased for drift-optimized configurations when ν is very low, and that drift optimization cannot be used to reduce the neoclassical losses throughout the entire *lmfp* regime [12,29]. However, more recent analytical and numerical results have contradicted these initial

findings [16,27]. In these latter results, certain drift-optimized stellarators continued to exhibit more favorable transport rates than their non-optimized counterparts even at very low ν, although the reduction was less than that found in the ν^{-1} regime.

To determine whether a particular device is drift optimized or not, it is usually sufficient to look at the signs of the coefficients of the principal helical harmonic ($C_{1,n}$,$S_{1,n}$) and its largest sideband ($C_{1,n\pm1}$,$S_{1,n\pm1}$). As a rule, if the signs are opposite the configuration will exhibit some degree of drift optimization; if the signs are the same the device is drift amplified. Applying this rule to the four configurations given in Figure 1, one can classify HS5V10N and LHD as drift optimized while W VII-A and U2M are drift amplified (which is typical for classical, continuously wound stellarators and torsatrons [30]). These four devices thus provide an excellent opportunity to clarify the neoclassical transport properties of drift-optimized/drift-amplified stellarators, using actual magnetic fields.

The Fourier decompositions of B given in Figure 1 also illustrate an important trait of Helias which is not typical of the majority of toroidal devices, namely that the magnitude of the toroidal modulation of B, $|C_{0,1}|$, is less than the inverse aspect ratio, $\epsilon_t \equiv r/R_0$, for each and every flux surface. The exact ratio of these two quantities depends on the particular Helias (and can approach zero for a quasi-helical Helias [4]); for HS5V10N one finds that $|C_{0,1}|/\epsilon_t \approx 0.4$. In contrast, one sees that the usual toroidal approximation $|C_{0,1}| = \epsilon_t$ is relatively accurate for the three remaining configurations. This difference has important consequences for the neoclassical transport coefficients as will be described below.

III. THE BOUNCE-AVERAGED KINETIC EQUATION AND ITS SOLUTION BY THE POWER-SERIES TECHNIQUE

In the *lmfp* regime the bounce frequency of particles trapped in the local helical-ripple wells of a stellarator's magnetic field is much greater than the frequency with which such particles are collisionally removed from the wells. As is well known, for these localized particles the quantity $\mathcal{J} = \oint v_\parallel dl$ is an adiabatic invariant of the motion. The subsequent simplification of the guiding-center drift-kinetic equation which this invariant allows yields the bounce-averaged kinetic equation [31]

$$\langle \dot{r} \rangle \frac{\partial F_m}{\partial r} + \langle \dot{\theta} \rangle \frac{\partial f}{\partial \theta} = \frac{\epsilon_h}{\epsilon_H} \frac{\nu_{eff}}{A'(k^2)} \frac{\partial}{\partial k^2} \Big(A(k^2) \frac{\partial f}{\partial k^2} \Big), \tag{4}$$

where $\langle \dot{r} \rangle$ and $\langle \dot{\theta} \rangle$ are the bounce-averaged radial drift velocity and poloidal precession frequency, respectively, and $\nu_{eff} = \nu/2\epsilon_h$ where ν is the 90 degree deflection frequency.

The "effective" collision frequency, ν_{eff}, is the frequency with which trapped particles are collisionally removed from the local ripple wells. $A(k^2) = 8(E(k) - (1-k^2)K(k))$ and $A'(k^2) = \partial A(k^2)/\partial k^2 = 4K(k)$ are functions of the complete elliptic integrals of the first, $K(k)$, and second, $E(k)$, kinds with the argument being the pitch-angle variable k^2, which is given by [11]

$$k^2 = \frac{\kappa/\mu B_0 - C_{0,0} + |C_{0,1}|\cos\theta - C_{0,2}\cos 2\theta + \epsilon_H}{2\epsilon_H},$$

where $\kappa = mv^2/2$ is the kinetic energy and $\mu = mv_\perp^2/2B$ is the magnetic moment. Localized particles satisfy $0 \leq k^2 < 1$, with the limits corresponding to particles trapped at the bottom of a helical-ripple well and to those marginally trapped, respectively.

Throughout this work it will be assumed that a large ambipolar potential, $\Phi(r)$, is present in the plasma. Given this assumption and the model magnetic field of Equation (2), the bounce-averaged drift velocities are given by

$$\begin{aligned} \langle \dot{r} \rangle &= \frac{v_d}{\epsilon_t}\sin\theta\Big(|C_{0,1}| - \sigma_1\epsilon_h\langle\cos\eta\rangle\Big) - \frac{2v_d}{\epsilon_t}\sin 2\theta\Big(C_{0,2} + \sigma_2\epsilon_h\langle\cos\eta\rangle\Big), \\ r\langle\dot{\theta}\rangle &\approx r\Omega_E = -\frac{(d\Phi/dr)}{B_0}, \end{aligned} \tag{5}$$

where $v_d = \mu/qR_0$ is the ∇B drift velocity, $\eta = \chi - p\phi$ and $\langle\cos\eta\rangle = 2E(k)/K(k) - 1$. The function $\langle\cos\eta\rangle$ satisfies $-1 \leq \langle\cos\eta\rangle \leq 1$, being positive for the great majority of k^2 values as is demonstrated in Figure 3.

Typically the first term in the radial drift velocity dominates and it is instructive to consider the properties of Equation (5) in this particular case. For the idealized model stellarator field $\langle\dot{r}\rangle = v_d\sin\theta$ is independent of a particle's depth in a helical-ripple well. However, this situation changes as soon as σ_1 assumes a non-zero value. For positive σ_1 values the radial drift velocity of all trapped particles with $k^2 < 0.83$ is reduced relative to the idealized case. (Clearly the relative drift velocity is increased for shallowly trapped particles, i.e. those particles which satisfy $k^2 > 0.83$.) It will be noted that the reduction in the radial drift is particularly effective for the most deeply trapped particles. As will be discussed later in more detail, these particles dominate the transport process in the ν^{-1} regime; this explains qualitatively why a drift-optimized stellarator is successful in reducing the transport level in this regime. If σ_1 becomes large enough so that $\sigma_1\epsilon_h \gtrsim |C_{0,1}|$ one must generally consider the full expression for $\langle\dot{r}\rangle$, as both terms in the radial drift velocity will be of comparable magnitude for a particular range of k^2 values.

In Equation (4) the distribution function has been expanded as a combination of a lowest-order Maxwellian, F_m, and a first-order perturbation, f. The usual transport ordering $\langle\dot{\theta}\rangle, \nu_{eff} \gg \langle\dot{r}\rangle/\delta r$, where δr is the radial scale length of the plasma, has also been assumed. To solve this equation without resorting to a further ordering scheme in the ratio of $\langle\dot{\theta}\rangle$ to ν_{eff}, it is assumed that the perturbed distribution function may be written

$$f = \frac{\partial F_m}{\partial r}\Big(Z(k^2) + Y(k^2)\sin\theta + X(k^2)\cos\theta + W(k^2)\sin 2\theta + V(k^2)\cos 2\theta\Big).$$

(The assumption that $\langle\dot{\theta}\rangle$ consists only of the $\mathbf{E}\times\mathbf{B}$ precession frequency has two notable consequences which should be mentioned here. First, it allows the termination of this Fourier *ansatz* for f at the 2θ terms; in the large Ω_E limit, higher-order harmonics, for which no nonhomogeneous terms appear in the kinetic equation, are found to have negligibly small magnitudes relative to the harmonics retained above. Second, it is possible to drop the term $\dot{k}^2(\partial f/\partial k^2)$ from Equation (4), which should otherwise appear on the left-hand side of the bounce-averaged kinetic equation [32]. It has been found that this term only plays a significant role when the ∇B contribution to $\langle\dot{\theta}\rangle$ is included in Equation (5) and when $\Omega_{\nabla B} \gtrsim \Omega_E$ [33].)

With the above *ansatz* for f, the bounce-averaged kinetic equation separates into a set of five coupled differential equations

$$\hat{\nu}\frac{A}{A'}Z'' + \hat{\nu}Z' + \frac{\sigma_1}{2}Y + \sigma_2 W = 0,$$

$$\hat{\nu}\frac{A}{A'}Y'' + \hat{\nu}Y' + \Big(1+\frac{\sigma_2}{2}\Big)X - \sigma_1 V =$$

$$\frac{v_d}{\Omega_E\epsilon_t}\Big(1+\frac{\sigma_2}{2}\Big)\Big(|C_{0,1}| - \sigma_1\epsilon_h\langle\cos\eta\rangle\Big) + \frac{v_d\sigma_1}{\Omega_E\epsilon_t}\Big(C_{0,2} + \sigma_2\epsilon_h\langle\cos\eta\rangle\Big),$$

$$\hat{\nu}\frac{A}{A'}X'' + \hat{\nu}X' - \Big(1-\frac{\sigma_2}{2}\Big)Y + \sigma_1 W = 0,$$

$$\hat{\nu}\frac{A}{A'}W'' + \hat{\nu}W' + 2V - \frac{\sigma_1}{2}X = -\frac{2v_d}{\Omega_E\epsilon_t}\Big(C_{0,2} + \sigma_2\epsilon_h\langle\cos\eta\rangle\Big) - \frac{v_d\sigma_1}{2\Omega_E\epsilon_t}\Big(|C_{0,1}| - \sigma_1\epsilon_h\langle\cos\eta\rangle\Big),$$

$$\hat{\nu}\frac{A}{A'}V'' + \hat{\nu}V' - 2W + \frac{\sigma_1}{2}Y = 0,$$

where $\hat{\nu} \equiv \nu_{eff}/\Omega_E$ and the primes denote differentiation with respect to k^2. These equations are then to be solved using the power-series-expansion technique, with

$$Z(k^2) = \sum_{n=0}^{\infty} Z_n (k^2)^n \ , \qquad Y(k^2) = \sum_{n=0}^{\infty} Y_n (k^2)^n \ , \qquad X(k^2) = \sum_{n=0}^{\infty} X_n (k^2)^n \ ,$$

$$W(k^2) = \sum_{n=0}^{\infty} W_n (k^2)^n \ , \qquad V(k^2) = \sum_{n=0}^{\infty} V_n (k^2)^n \ .$$

To implement the power-series approach it is necessary to have $A(k^2)/A'(k^2)$ and $\langle \cos\eta \rangle$ expressed in powers of k^2. Both of these quantities depend on the ratio $E(k)/K(k)$. In principle, it is therefore possible to take the power-series expansions of the complete elliptic integrals and, in turn, to construct the series expansion of this ratio

$$\frac{E(k)}{K(k)} = 1 - \frac{k^2}{2} - \frac{(k^2)^2}{16} - \frac{(k^2)^3}{32} - \frac{41(k^2)^4}{2048} - \frac{59(k^2)^5}{4096} - \cdots \ .$$

In practice, however, such an approach leads to a double infinite sum in the differential equations and greatly complicates their solution. This difficulty was avoided in Reference [16] by truncating the $E(k)/K(k)$ expansion at the first power of k^2, yielding the approximations $A(k^2)/A'(k^2) = k^2$ and $\langle \cos\eta \rangle = 1 - k^2$; a particularly simple set of recursion relationships ultimately followed from these approximations. However, in light of the physical processes which the bounce-averaged kinetic equation is meant to describe, these approximations appear somewhat suspect. In particular, for drift-amplified and drift-optimized configurations, the assumption for $\langle \cos\eta \rangle$ has the consequence of increasing or reducing, respectively, the radial drift velocity of *all* ripple-trapped particles *including* those which are shallowly trapped.

The most obvious remedy to this shortcoming is to keep higher-order terms in the expansion of $E(k)/K(k)$. Unfortunately, the convergence of this series is not rapid, owing to the logarithmic singularity of $K(k)$ at $k^2 = 1$, and a large number of terms is required to obtain a reasonably accurate expression. Instead, in the present work, it will be assumed that

$$\frac{A(k^2)}{A'(k^2)} = k^2 - \frac{\xi (k^2)^2}{4} \ , \qquad \langle \cos\eta \rangle = 1 - k^2 - \frac{\xi (k^2)^2}{4} \ . \tag{6}$$

The quantity ξ in Equation (6) serves as both a tag and a switch (having a value of either one or zero), identifying terms that were not present in the solution of Reference [16] and allowing for quick recovery of those results by setting $\xi = 0$. Not only are these

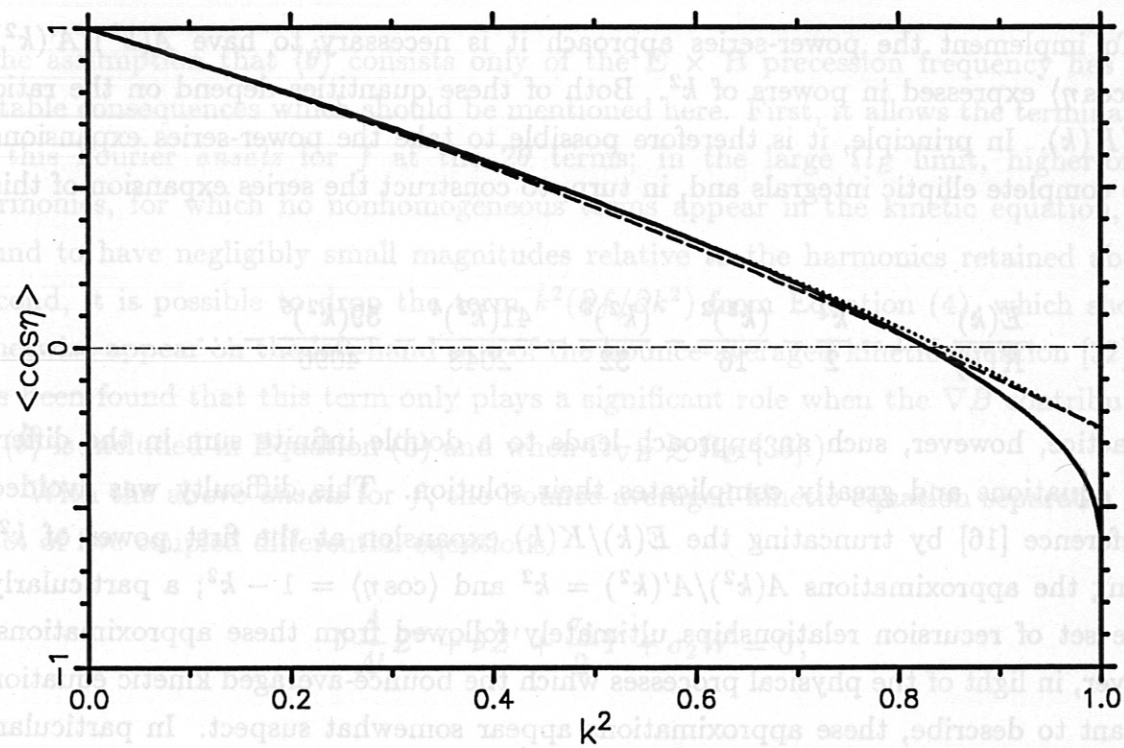

Figure 3. The bounce-averaged ripple phase $\langle \cos\eta \rangle = 2E(k)/K(k) - 1$ *is plotted as a function of the pitch-angle variable* k^2 *(solid line). Also shown are two approximations for* $\langle \cos\eta \rangle$*; Equation (6) with* $\xi = 1$ *(broken line) and the result obtained by employing the series expansions of the complete elliptic integrals and retaining terms through* $(k^2)^5$ *(dotted line).*

expressions simple, they are also relatively accurate as is shown for $\langle \cos\eta \rangle$ by the broken line in Figure 3 (note that both the actual and approximate curves pass through zero at $k^2 = 0.83$). Also given in this figure by the dotted line is the approximation for $\langle \cos\eta \rangle$ obtained by employing the series expansion of $E(k)/K(k)$ through the $(k^2)^5$ term. As can be seen, this approximation is very little better than that given in Equation (6), illustrating the slow convergence of this series.

Making these substitutions, one finds that the series may be expressed

$$Z(k^2) = Z_0 + \sum_{n=0}^{\infty} (k^2)^n \left(z_n^{(Z)} + y_n^{(Z)} Y_0 + x_n^{(Z)} X_0 + w_n^{(Z)} W_0 + v_n^{(Z)} V_0 \right),$$

$$Y(k^2) = \sum_{n=0}^{\infty} (k^2)^n \left(z_n^{(Y)} + y_n^{(Y)} Y_0 + x_n^{(Y)} X_0 + w_n^{(Y)} W_0 + v_n^{(Y)} V_0 \right),$$

$$X(k^2) = \sum_{n=0}^{\infty} (k^2)^n \left(z_n^{(X)} + y_n^{(X)} Y_0 + x_n^{(X)} X_0 + w_n^{(X)} W_0 + v_n^{(X)} V_0 \right),$$

$$W(k^2) = \sum_{n=0}^{\infty} (k^2)^n \left(z_n^{(W)} + y_n^{(W)} Y_0 + x_n^{(W)} X_0 + w_n^{(W)} W_0 + v_n^{(W)} V_0 \right),$$

$$V(k^2) = \sum_{n=0}^{\infty} (k^2)^n \left(z_n^{(V)} + y_n^{(V)} Y_0 + x_n^{(V)} X_0 + w_n^{(V)} W_0 + v_n^{(V)} V_0 \right),$$

where the constituent parts of $Z(k^2)$ are given by the recursion formula

$$q_n^{(Z)} = \frac{-(\sigma_1/2) q_{n-1}^{(Y)} - \sigma_2 q_{n-1}^{(W)}}{\hat{\nu} n^2} + \frac{\xi (n-1)(n-2) q_{n-1}^{(Z)}}{4n^2}, \qquad q = z, y, x, w, v$$

the constituent parts of $Y(k^2)$ are given by the recursion formulae

$$z_n^{(Y)} = \frac{-(1+\sigma_2/2) z_{n-1}^{(X)} + \sigma_1 z_{n-1}^{(V)} + a_n^{(Y)}}{\hat{\nu} n^2} + \frac{\xi (n-1)(n-2) z_{n-1}^{(Y)}}{4n^2},$$

$$q_n^{(Y)} = \frac{-(1+\sigma_2/2) q_{n-1}^{(X)} + \sigma_1 q_{n-1}^{(V)}}{\hat{\nu} n^2} + \frac{\xi (n-1)(n-2) q_{n-1}^{(Y)}}{4n^2}, \qquad q = y, x, w, v$$

with

$$a_1^{(Y)} = \frac{v_d}{\Omega_E}\frac{|C_{0,1}|}{\epsilon_t}\left(1+\frac{\sigma_2}{2}\right) - \frac{v_d}{\Omega_E}\frac{\epsilon_h}{\epsilon_t}\sigma_1\left(1-\frac{\sigma_2}{2}-\frac{C_{0,2}}{\epsilon_h}\right),$$

$$a_2^{(Y)} = \frac{v_d}{\Omega_E}\frac{\epsilon_h}{\epsilon_t}\sigma_1\left(1-\frac{\sigma_2}{2}\right),$$

$$a_3^{(Y)} = \left(\frac{\xi}{4}\right)a_2^{(Y)},$$

$$a_n^{(Y)} = 0\,, \qquad n > 3$$

the constituent parts of $X(k^2)$ are given by the recursion formula

$$q_n^{(X)} = \frac{(1-\sigma_2/2)q_{n-1}^{(Y)} - \sigma_1 q_{n-1}^{(W)}}{\hat{\nu}n^2} + \frac{\xi(n-1)(n-2)q_{n-1}^{(X)}}{4n^2}, \qquad q = z, y, x, w, v$$

the constituent parts of $W(k^2)$ are given by the recursion formulae

$$z_n^{(W)} = \frac{-2z_{n-1}^{(V)} + (\sigma_1/2)z_{n-1}^{(X)} + a_n^{(W)}}{\hat{\nu}n^2} + \frac{\xi(n-1)(n-2)z_{n-1}^{(W)}}{4n^2},$$

$$q_n^{(W)} = \frac{-2q_{n-1}^{(V)} + (\sigma_1/2)q_{n-1}^{(X)}}{\hat{\nu}n^2} + \frac{\xi(n-1)(n-2)q_{n-1}^{(W)}}{4n^2}, \qquad q = y, x, w, v$$

with

$$a_1^{(W)} = \frac{-2v_d}{\Omega_E\epsilon_t}\left(C_{0,2} + \sigma_2\epsilon_h + \frac{\sigma_1}{4}(|C_{0,1}| - \sigma_1\epsilon_h)\right),$$

$$a_2^{(W)} = \frac{v_d}{\Omega_E}\frac{\epsilon_h}{\epsilon_t}\left(2\sigma_2 - \frac{\sigma_1^2}{2}\right),$$

$$a_3^{(W)} = \left(\frac{\xi}{4}\right)a_2^{(W)},$$

$$a_n^{(W)} = 0\,, \qquad n > 3$$

the constituent parts of $V(k^2)$ are given by the recursion formula

$$q_n^{(V)} = \frac{2q_{n-1}^{(W)} - (\sigma_1/2)q_{n-1}^{(Y)}}{\hat{\nu}n^2} + \frac{\xi(n-1)(n-2)q_{n-1}^{(V)}}{4n^2}, \qquad q = z, y, x, w, v$$

and the $n = 0$ coefficients have the values

$$z_0^{(Z)} = 0, \quad y_0^{(Z)} = 0, \quad x_0^{(Z)} = 0, \quad w_0^{(Z)} = 0, \quad v_0^{(Z)} = 0,$$

$$z_0^{(Y)} = 0, \quad y_0^{(Y)} = 1, \quad x_0^{(Y)} = 0, \quad w_0^{(Y)} = 0, \quad v_0^{(Y)} = 0,$$

$$z_0^{(X)} = 0, \quad y_0^{(X)} = 0, \quad x_0^{(X)} = 1, \quad w_0^{(X)} = 0, \quad v_0^{(X)} = 0,$$

$$z_0^{(W)} = 0, \quad y_0^{(W)} = 0, \quad x_0^{(W)} = 0, \quad w_0^{(W)} = 1, \quad v_0^{(W)} = 0,$$

$$z_0^{(V)} = 0, \quad y_0^{(V)} = 0, \quad x_0^{(V)} = 0, \quad w_0^{(V)} = 0, \quad v_0^{(V)} = 1.$$

THE BOUNDARY CONDITIONS

To complete the solution, boundary conditions at $k^2 = 1$ are needed to determine the five unknowns, Z_0, Y_0, X_0, W_0 and V_0. For this purpose, the most rigorous way to proceed is to determine a solution of the *ripple-averaged* kinetic equation for non-localized particles; continuity requirements then unambiguously set the boundary conditions. This has been the approach favored in numerical solutions of the bounce-averaged/ripple-averaged kinetic equation [27,32,34]. (The terminology "ripple-averaged" has been adopted here since, of course, non-localized particles do not "bounce" in the stellarator's helical ripples. Formally, both averages are time averages, the bounce average over the periodic motion of localized particles and the ripple average over the time it takes a non-localized particle to traverse a single helical-ripple well — see Reference [32] for a thorough physical and mathematical presentation.)

This is also the approach that will be adopted here, although in an approximate form. First, it will be assumed that the orbits of non-localized particles are completely described by the parallel motion along field lines, the so-called *zero-banana-width* approximation. This is equivalent to ignoring all "axisymmetric" transport processes and is a common simplifying assumption in the *lmfp* regime, where the transport due to locally trapped particles generally dominates the overall transport rate. Second, and most importantly, use will be made of the fact that $\langle\dot{\theta}\rangle_r = \iota\langle v_\parallel\rangle_r/R \gg \nu_{eff}$ in the *lmfp* regime (where the r subscript denotes that the quantities in brackets have been ripple averaged and ι is the rotational transform), so that a first approximation to f

may be obtained from a "collisionless" kinetic equation. With these two assumptions the kinetic equation for non-localized particles may be expressed

$$\langle \dot{\theta} \rangle_r \frac{\partial f}{\partial \theta} + \dot{k}^2 \frac{\partial f}{\partial k^2} = 0.$$

The zero-banana-width approximation also allows one to immediately write $\dot{k}^2 = (\partial k^2/\partial \theta)\langle \dot{\theta} \rangle_r$ and further simplify the kinetic equation

$$\frac{\partial f}{\partial \theta} + \frac{\partial k^2}{\partial \theta} \frac{\partial f}{\partial k^2} = 0. \tag{7}$$

It is perhaps not immediately apparent why one should expect any solution to this equation other than the trivial $f = 0$, and indeed this result has been employed by numerous authors. The trivial solution neglects, however, the effects of collisionless trapping/detrapping due to "transition" particles which, in the course of their collisionless orbits, alternate between being ripple trapped and toroidally blocked (executing tokamak-banana-like orbits). As these transition particles play a crucial role at very-low values of collision frequency [28], it is necessary to obtain a solution of Equation (7) which accounts for their presence.

To proceed, it will once again be useful to consider the limiting case $C_{0,2} = \sigma_2 = 0$, for which

$$\frac{\partial k^2}{\partial \theta} = -\sin\theta \, \frac{\left(|C_{0,1}| + \sigma_1 \epsilon_h (2k^2 - 1)\right)}{2\epsilon_h \left(1 - \sigma_1 \cos\theta\right)},$$

and for which Equation (7) has two possible solutions, depending on the value of σ_1

I. $-\dfrac{|C_{0,1}|}{\epsilon_h} \leq \sigma_1 \leq 1$

$$f(k^2 \geq 1, \theta) = \left\{ \begin{array}{ll} \mathcal{C}_{\rm I} \left(\dfrac{|C_{0,1}| + \sigma_1 \epsilon_h (2k^2 - 1)}{2\epsilon_h (1 - \sigma_1 \cos\theta)^{-1}} \right)^{-\mathcal{G}}, & |C_{0,1}| + \sigma_1 \epsilon_h (2k^2 - 1) \geq 0 \\ 0, & |C_{0,1}| + \sigma_1 \epsilon_h (2k^2 - 1) \leq 0 \end{array} \right\}$$

II. $-1 \leq \sigma_1 \leq -\dfrac{|C_{0,1}|}{\epsilon_h}$

$$f(k^2 \geq 1, \theta) = \mathcal{C}_{\rm II} \left(\frac{-|C_{0,1}| - \sigma_1 \epsilon_h (2k^2 - 1)}{2\epsilon_h (1 - \sigma_1 \cos\theta)^{-1}} \right)^{-\mathcal{H}}$$

where $\mathcal{G} = a_{\rm I}(1 - \sigma_1)/\sigma_1$, $\mathcal{H} = -a_{\rm II}(1 + \sigma_1)/\sigma_1$, and $\mathcal{C}_{\rm I}$, $a_{\rm I}$, $\mathcal{C}_{\rm II}$ and $a_{\rm II}$ are constants to be determined. Note that the latter of these solutions is only possible when $|C_{0,1}| < \epsilon_h$,

and even then it is unlikely to hold for realistic magnetic-field configurations since the condition $-1 \leq \sigma_1 \leq -|C_{0,1}|/\epsilon_h$ requires that the absolute maximum of B occur on the outside ($\theta = 0$) of the device. For this reason, this solution will not be considered further here.

The solution is clearly even in θ; indeed, using the binomial series expansion, the poloidal dependence of f may be recast in the form of a Fourier cosine series. Doing so, and requiring continuity of f at $k^2 = 1$, the (non-trivial) solution for non-localized particles becomes

$$f(k^2 \geq 1, \theta) = \frac{\Big(|C_{0,1}| + \sigma_1 \epsilon_h\Big)^{\mathcal{G}}}{\Big(|C_{0,1}| + \sigma_1 \epsilon_h (2k^2 - 1)\Big)^{\mathcal{G}}} \Big(Z(1) + X(1)\cos\theta + V(1)\cos 2\theta\Big) \frac{\partial F_m}{\partial r} ,$$

where the θ dependence of this result has been truncated to correspond with the *ansatz* made earlier for localized particles. Continuity of the distribution function also immediately yields two boundary conditions on the portion of f which is odd in θ, namely

$$Y(1) = W(1) = 0 .$$

To determine the remaining boundary conditions, continuity of $\partial f/\partial k^2$ at $k^2 = 1$ is invoked; given the assumptions and simplifications which led to Equation (7), however, this requirement must be restricted to the *even* part of f. To see why this is so, it is instructive to consider the results from numerical simulations [27,32,34], where the full ripple-averaged kinetic equation (including the collision operator and the source term due to the radial particle drift) is solved for non-localized particles. These simulations have shown that the distribution function for non-localized particles is indeed symmetric with the exception of a thin boundary layer of width $\Delta k^2 \approx (\nu_{eff}/\langle\dot{\theta}\rangle_r)^{1/2}$ just above $k^2 = 1$ which is necessary to insure that the asymmetric portion of the true $\partial f/\partial k^2 \approx \Delta f/\Delta k^2$ is continuous (this continuity condition also demands that the removal of the asymmetry in f takes place largely below $k^2 = 1$ due to the great disparity in Ω_E and $\langle\dot{\theta}\rangle_r$). Thus, the boundary conditions $Y(1) = W(1) = 0$ are a reasonable approximation to the numerical results (these approximations improve with decreasing collision frequency) even though $Y'(1)$ and $W'(1)$ will be non-negligible in value. Clearly, solutions of Equation (7) cannot reproduce this behavior since collisions have been neglected, and thus continuity of $\partial f/\partial k^2$ is limited to the even portion of f

$$\begin{bmatrix} Z(1) \\ X(1) \\ V(1) \end{bmatrix} = -\frac{\big(|C_{0,1}| + \sigma_1 \epsilon_h\big)}{2a_1 \epsilon_h (1 - \sigma_1)} \begin{bmatrix} Z'(1) \\ X'(1) \\ V'(1) \end{bmatrix} \tag{8}$$

where column vectors have been employed for notational convenience.

These boundary conditions are satisfying from a physical viewpoint but leave the constant $a_{\rm I}$ undetermined. In this respect, the numerical simulation of Reference [34] may once again be of help. This simulation employs an idealized model magnetic field — that of Equation (3) with $\sigma_1 = 0$ — in which case the multiplicative term of Equation (8) becomes $-\epsilon_t/(2a_{\rm I}\epsilon_h)$. The boundary conditions then reduce to those found heuristically in Reference [16] for the same idealized magnetic field if one sets $a_{\rm I} = 1$. The numerical results confirm the validity of these boundary conditions with the exception that $a_{\rm I}$ is found to have a value of two; for this reason, $a_{\rm I} = 2$ will be taken here as well.

These boundary conditions are best understood from a physical standpoint by considering the trajectories of transition particles during the toroidally blocked portion of their orbits. For such particles, detrapping at arbitrary poloidal angle $\theta = \theta_d$, the "distance" (measured in terms of k^2) above the trapping/detrapping boundary at any value of θ is given by

$$k^2 - 1 = \frac{(\,|C_{0,1}| + \sigma_1\epsilon_h)(\cos\theta - \cos\theta_d)}{2\epsilon_h(1 - \sigma_1\cos\theta)}.$$

It is easy to show that this quantity is maximized at $\theta = 0$ where

$$(k^2 - 1)_{\rm max} = \frac{(\,|C_{0,1}| + \sigma_1\epsilon_h)(1 - \cos\theta_d)}{2\epsilon_h(1 - \sigma_1)}.$$

Further, by once again using the binomial series expansion, the pitch-angle dependence of $f(k^2 \geq 1, \theta)$ near $k^2 = 1$ may be written as

$$\exp\left\{-\frac{2a_{\rm I}\epsilon_h(1-\sigma_1)}{|C_{0,1}| + \sigma_1\epsilon_h}(k^2 - 1)\right\} + 2a_{\rm I}\sigma_1(1-\sigma_1)\left\{\frac{\epsilon_h(k^2-1)}{|C_{0,1}| + \sigma_1\epsilon_h}\right\}^2 + \cdots,$$

the leading term of which describes exponential decay with a k^2 scale length given approximately by $(k^2-1)_{\rm max}$. In other words, in the vicinity of the trapping/detrapping boundary $k^2 = 1$, the solution of the kinetic equation for the non-localized distribution function decays exponentially with a scale length set by transition particles in the toroidally blocked portion of their orbits, and hence one obtains the boundary conditions given in Equation (8).

For non-zero $C_{0,2}$ and σ_2 a general solution of the type just obtained is not possible. For parameters of interest, however, it is possible to use the approximate solution

$$f(k^2 \geq 1, \theta) = C_{\rm I}\left(\frac{|C_{0,1}| - 3C_{0,2} + (\sigma_1\epsilon_h + 3\sigma_2\epsilon_h)(2k^2 - 1)}{2\epsilon_h(1 - \sigma_1\cos\theta - \sigma_2\cos 2\theta)^{-1}}\right)^{-\mathcal{G}},$$

$$|C_{0,1}| - 3C_{0,2} + (\sigma_1\epsilon_h + 3\sigma_2\epsilon_h)(2k^2 - 1) \geq 0$$

$$f(k^2 \geq 1, \theta) = 0\,, \qquad |C_{0,1}| - 3C_{0,2} + (\sigma_1\epsilon_h + 3\sigma_2\epsilon_h)(2k^2 - 1) \leq 0$$

with $\mathcal{G} = 2(1-\sigma_1-\sigma_2)/(\sigma_1+3\sigma_2)$. This solution is exact for $\sigma_1 C_{0,2} + \sigma_2 |C_{0,1}| = 0$ and is reasonably accurate as long as this quantity is small with respect to $2\epsilon_h$. Applying the boundary conditions, one finds that, as before, the odd part of f vanishes at $k^2 = 1$ and that

$$\begin{bmatrix} Z(1) \\ X(1) \\ V(1) \end{bmatrix} = -\frac{\left(|C_{0,1}| + \sigma_1\epsilon_h + 3(\sigma_2\epsilon_h - C_{0,2})\right)}{4\epsilon_h(1-\sigma_1-\sigma_2)} \begin{bmatrix} Z'(1) \\ X'(1) \\ V'(1) \end{bmatrix}.$$

These are the boundary conditions which will be employed throughout the remainder of this paper.

The power-series solution of the bounce-averaged kinetic equation may be implemented computationally with little difficulty. Beginning from the recursion formulae, one calculates the individual $q_n^{(Q)}$ ($q = z, y, x, w, v$; $Q = Z, Y, X, W, V$) successively until the value of n is reached where each $q_n^{(Q)}$ is a very small fraction of the characteristic diffusive step size Δr (where Δr depends on collision frequency, being the smaller of $(|C_{0,1}|/\epsilon_t)(v_d/\nu_{eff})$ and $(|C_{0,1}|/\epsilon_t)(v_d/\Omega_E)$). For $\hat{\nu} > 1$ convergence is rapid — $n = 10$ at most — while, on the other hand, the number of terms required for convergence steadily increases as the collision frequency becomes smaller. Once the individual $q_n^{(Q)}$ have been determined it is straightforward to apply the boundary conditions and determine the unknown constants Z_0, Y_0, X_0, W_0 and V_0.

With the power-series solution for f complete it is possible to calculate the expected particle and heat fluxes

$$\begin{bmatrix} \Gamma \\ Q \end{bmatrix} = -4\pi\left(\frac{2}{m^3}\right)^{1/2} \int d\kappa \begin{bmatrix} \kappa^{1/2} \\ \kappa^{3/2} \end{bmatrix} D(\kappa) \frac{\partial F_m}{\partial r},$$

where the diffusion coefficient is given by

$$D(\kappa) = -\frac{1}{\pi^2} \int_0^{2\pi} d\theta \int_0^1 dk^2 \left(\frac{\epsilon_H}{2}\right)^{1/2} \langle \dot{r} \rangle \left(Y(k^2)\sin\theta + W(k^2)\sin 2\theta\right) K(k). \quad (9)$$

It will be noted in the above expression that only the portion of f which is odd in θ contributes directly to the fluxes. The remaining analytic calculations given in this paper will therefore concentrate on determining expressions for $Y(k^2)$ and $W(k^2)$ in various asymptotic limits, while largely ignoring the even part of f.

IV. ASYMPTOTIC SOLUTIONS OF THE BOUNCE-AVERAGED KINETIC EQUATION AND THEIR PROPERTIES

The power-series solution of the bounce-averaged kinetic equation, described in the preceeding section, has the great advantage that it is valid throughout the entire *lmfp* regime and not simply for a particular ordering of $\nu_{eff}/\langle\dot{\theta}\rangle$. Thus, it not only describes the "high" ($\nu_{eff} \gg \Omega_E$, 'ν^{-1} regime' [31,35]), "low" ($\nu_{eff} \ll \Omega_E$, 'ν regime' [28]) and "intermediate" ($\nu_{eff} \lesssim \Omega_E$, '$\nu^{1/2}$ regime' [31,36]) collision-frequency regimes of classical stellarator theory, it also handles the transitions between these regimes. The additional fact that the power-series solution has been developed for a helical-ripple profile of the form $\epsilon_H = \epsilon_h(1 - \sigma_1 \cos\theta - \sigma_2 \cos 2\theta)$ also means that it may be applied to a large number of realistic stellarator configurations.

Despite these advantages, the complexity of the power-series solution and the large number of terms which is often required for convergence can be drawbacks, for example if one wishes to determine the precise scaling of the transport coefficients with respect to such parameters as σ_1 and σ_2. For this purpose it is worthwhile in this section to employ the more conventional technique of solving Equation (4) in successive orders of a small expansion parameter, a method which has been used successfully by several authors to examine neoclassical transport in stellarators with θ-dependent ripple profiles [11-13,23] (but not necessarily with the form of ϵ_H used in this work). These papers have tended to concentrate on calculating the particle and heat fluxes for a given magnetic field configuration and have placed much less emphasis on determining the perturbed distribution function and investigating its properties. Qualitative explanations of the decrease (or increase) of the transport rates in drift-optimized stellarators have focused on the decrease (increase) of the radial drift velocity which a particular segment of the localized-particle population experiences [10,12,29]; these arguments have been touched on briefly earlier in this paper. Although it is perhaps obvious that a change in $\langle\dot{r}\rangle$ also leads to an alteration of the perturbed distribution function, this effect has been largely ignored.

In this section a somewhat different tack will be taken. The bounce-averaged kinetic equation will be solved for $f(\theta, k^2)$ (without approximations for the functions of complete elliptic integrals) in the $\nu_{eff} \gg \Omega_E$ limit, and in the opposite limit the behavior of the odd part of f for deeply trapped particles will be examined. In both cases, particular attention will be drawn to the effects of drift optimization/amplification, effects which will later prove to be of importance in explaining the unique transport characteristics of the Helias concept. This approach has the additional advantage of allowing a detailed comparison with the results of the power-series solution.

In the "high" collision-frequency limit a subsidiary ordering of the perturbed distribution function is possible, $f = f_0 + f_1 + \cdots$, where the subscript indicates the order of the small parameter Ω_E/ν_{eff}. Substituting into Equation (4), the lowest-order kinetic equation becomes

$$\frac{\epsilon_H}{\epsilon_h}\frac{\langle \dot{r} \rangle}{\nu_{eff}}\frac{\partial F_m}{\partial r} = \frac{1}{A'(k^2)}\frac{\partial}{\partial k^2}\left(A(k^2)\frac{\partial f_0}{\partial k^2}\right).$$

The solution to this equation will be odd in θ (since $\langle \dot{r} \rangle$ is odd in θ), hence $f_0(1) = 0$ is the appropriate boundary condition at $k^2 = 1$. Also requiring that f_0 be regular at $k^2 = 0$, one obtains the solution

$$f_0(\theta, k^2) = \frac{\epsilon_H}{\epsilon_h}\frac{v_d}{\nu_{eff}}\left(\Psi_1(k^2)\sin\theta + 2\Psi_2(k^2)\sin 2\theta\right)\frac{\partial F_m}{\partial r}$$

with

$$\begin{aligned}\Psi_1(k^2) &= \frac{|C_{0,1}|}{\epsilon_t}(k^2-1) + \frac{\sigma_1\epsilon_h}{3\epsilon_t}\left(k^2 - 1 + \pi - 2I(k^2)\right), \\ \Psi_2(k^2) &= -\frac{C_{0,2}}{\epsilon_t}(k^2-1) + \frac{\sigma_2\epsilon_h}{3\epsilon_t}\left(k^2 - 1 + \pi - 2I(k^2)\right),\end{aligned} \tag{10}$$

and where the function $I(k^2)$ is given by

$$I(k^2) = \int_0^{k^2} d\hat{k}^2 \frac{\hat{k}^2 E(\hat{k})}{E(\hat{k}) - (1-\hat{k}^2)K(\hat{k})} \approx 2k^2 - \frac{3(k^2)^2}{8} - \frac{(k^2)^3}{32} - \frac{21(k^2)^4}{2048}$$

and is plotted in Figure 4. The approximation for $I(k^2)$ has once again been obtained from the series expansions of $K(k)$ and $E(k)$ and is also shown for comparison.

Using the expressions for Ψ_1 and Ψ_2, one may investigate the k^2 dependence of f_0 in Helias and compare it with that of conventional stellarator-type devices. An example is given in Figure 5 for the idealized stellarator magnetic field ($|C_{0,1}| = \epsilon_t$, $C_{0,2} = \sigma_1 = \sigma_2 = 0$) and for the four configurations introduced in Section II. Also shown for comparison are the power-series-solution equivalents

$$\Psi_1 = \frac{\nu_{eff}}{v_d}\frac{4Y(k^2) + 2\sigma_1 W(k^2)}{(4 - \sigma_1^2 + 2\sigma_2)}, \qquad \Psi_2 = \frac{\nu_{eff}}{v_d}\frac{(2+\sigma_2)W(k^2) + \sigma_1 Y(k^2)}{(4 - \sigma_1^2 + 2\sigma_2)},$$

for $\xi = 1$ (broken line) and $\xi = 0$ (dotted line). The latter curves show that the power-series results are relatively insensitive to the approximations used for the functions of complete elliptic integrals. For $\xi = 1$, the analytical and power-series results for Ψ_1 show excellent agreement in all cases; the modest discrepancies in the Ψ_2 curves are due to the truncation of the power-series *ansatz* for f at the 2θ terms. The following points should be noted:

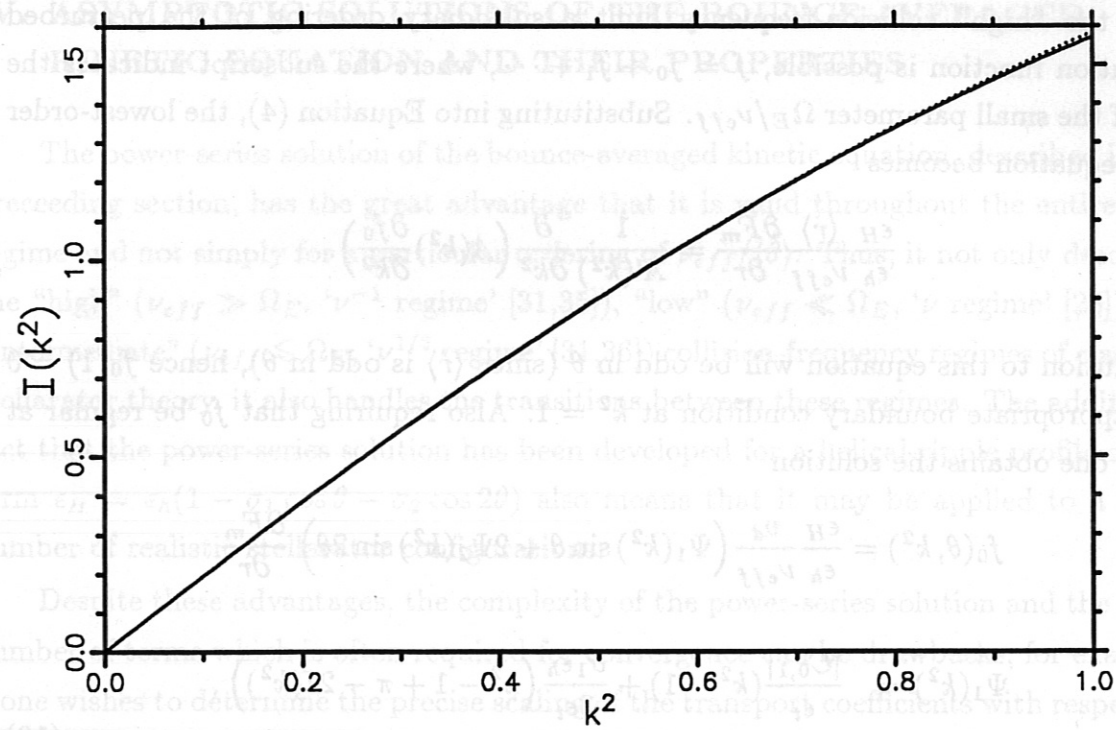

Figure 4. The function $I(k^2)$ which appears in the solution for f_0 is given by the solid line. Also shown (by the dotted line) is the polynomial approximation for $I(k^2)$ which appears in the text.

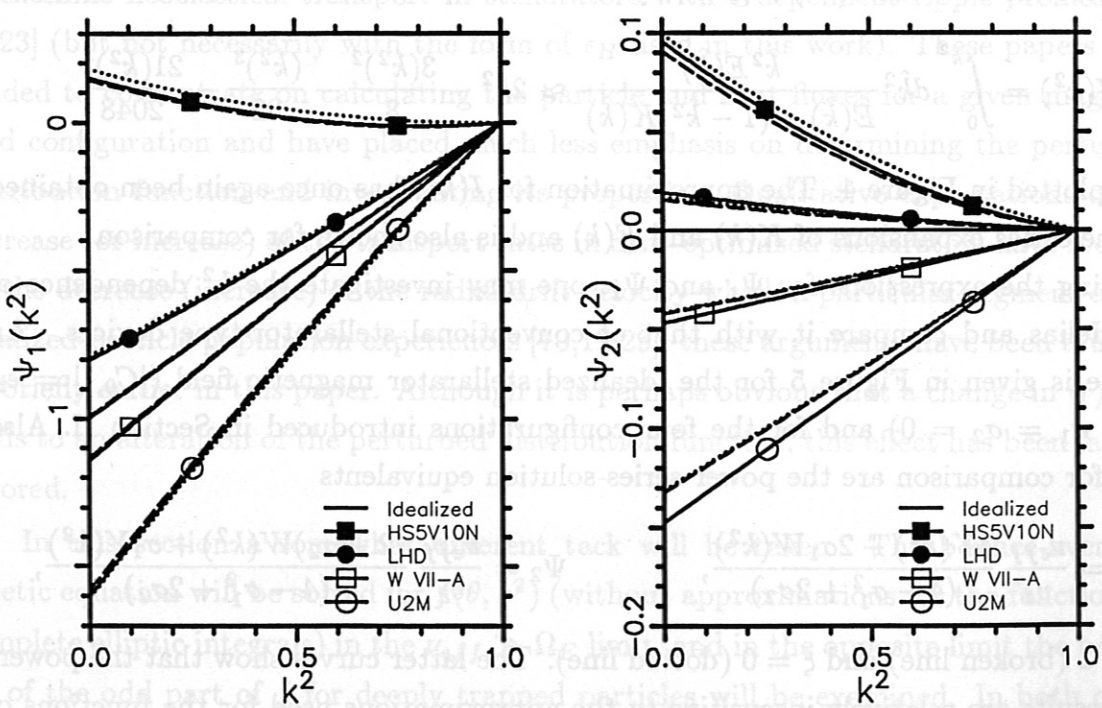

Figure 5. $\Psi_1(k^2)$ and $\Psi_2(k^2)$ are plotted for an idealized stellarator, HS5V10N, LHD, W VII-A and U2M; results are for the $\rho = 0.5$ flux surface. The solid lines are obtained from Equation (10) while the power-series-solution equivalents are given by the broken lines (for $\xi = 1$) and the dotted lines (for $\xi = 0$).

• For the idealized stellarator $\Psi_1 = k^2 - 1$. The results for LHD, W VII-A and U2M also show approximately linear dependence of Ψ_1 on k^2, but with an increase or decrease in the slope of the curve. In other words, the relative changes in Ψ_1 are roughly the same for all trapped particles.

• HS5V10N clearly does not fit this mold. It is also the only example for which the magnitudes of Ψ_1 and Ψ_2 are comparable, illustrating the importance for Helias of $C_{0,2}$ and σ_2 in the model magnetic field of Equation (2).

To further help in clarifying the effects that drift optimization/amplification has on neoclassical transport rates, it is useful to introduce the (normalized) poloidal average of the drift-weighted distribution function,

$$g_0(k^2) = \frac{\nu_{eff}}{v_d^2}\frac{1}{\pi}\int_0^{2\pi} d\theta \, \langle \dot{r} \rangle \, f_0 \left(\frac{\epsilon_H}{\epsilon_h}\right)^{1/2} \left(\frac{\partial F_m}{\partial r}\right)^{-1}.$$

This quantity represents the principal k^2 dependence appearing in the particle and heat flux integrals and thus indicates to what extent the different segments of the ripple-trapped-particle population contribute to the transport level. Taking the solution for f_0 and performing the necessary integration, one finds

$$g_0(k^2) = \frac{|C_{0,1}| - \sigma_1 \epsilon_h \langle \cos\eta \rangle}{\epsilon_t}\left\{\Psi_1\left(1 + \frac{3}{4}\sigma_2 + \frac{3}{32}\sigma_1^2 + \frac{3}{16}\sigma_2^2 - \frac{3}{128}\sigma_2^3 + \cdots\right)\right.$$
$$\left. + \frac{\sigma_1}{2}\Psi_2\left(-3 + \frac{1}{16}\sigma_1^2 + \frac{3}{32}\sigma_2^2 + \cdots\right)\right\}$$
$$- \frac{C_{0,2} + \sigma_2 \epsilon_h \langle \cos\eta \rangle}{\epsilon_t}\left\{\Psi_2\left(4 + \frac{3}{4}\sigma_1^2 + \frac{3}{8}\sigma_2^2 + \frac{3}{32}\sigma_1^2\sigma_2 + \cdots\right)\right.$$
$$\left. + \frac{\sigma_1}{2}\Psi_1\left(-3 + \frac{1}{16}\sigma_1^2 + \frac{3}{32}\sigma_2^2 + \cdots\right)\right\}.$$

Alternately, for the power-series solution of the kinetic equation, one obtains the result

$$g_0(k^2) = \frac{|C_{0,1}| - \sigma_1 \epsilon_h \langle \cos\eta \rangle}{\epsilon_t (v_d/\nu_{eff})}\left\{Y(k^2)\left(1 + \frac{1}{4}\sigma_2 - \frac{1}{32}\sigma_1^2 - \frac{1}{16}\sigma_2^2 + \frac{3}{128}\sigma_2^3 + \cdots\right)\right.$$
$$\left. - \frac{\sigma_1}{4}W(k^2)\left(1 + \frac{1}{16}\sigma_1^2 + \frac{3}{32}\sigma_2^2 + \cdots\right)\right\}$$
$$- \frac{C_{0,2} + \sigma_2 \epsilon_h \langle \cos\eta \rangle}{\epsilon_t (v_d/\nu_{eff})}\left\{W(k^2)\left(2 - \frac{1}{8}\sigma_1^2 - \frac{1}{16}\sigma_2^2 - \frac{3}{64}\sigma_1^2\sigma_2 + \cdots\right)\right.$$
$$\left. - \frac{\sigma_1}{2}Y(k^2)\left(1 + \frac{1}{16}\sigma_1^2 + \frac{3}{32}\sigma_2^2 + \cdots\right)\right\}.$$

Both of these expressions are illustrated in Figure 6 for the given magnetic-field configurations.

Previously it was asserted — based on the harmonic content of the respective magnetic fields — that HS5V10N and LHD should exhibit some degree of drift optimization while, conversely, W VII-A and U2M are drift-amplified devices. This assertion is confirmed through the results presented in Figure 6 by reduced (HS5V10N, LHD) and increased (W VII-A, U2M) values of $|g_0|$ relative to those of the idealized stellarator. This figure also illustrates the following points:

- The idealized stellarator represents the simplest case since here the radial drift velocity of a trapped particle is independent of its depth in a local ripple; this leads to $g_0 = k^2 - 1$, i.e. deeply trapped particles contribute most substantially to the transport simply because they have the chance to drift the furthest before being collisionally removed from the ripple.
- Drift optimization of conventional stellarator-type devices such as LHD is effective precisely because $\langle \dot{r} \rangle$ is smallest for deeply trapped particles. Conversely, for the drift-amplified configurations W VII-A and U2M, $\langle \dot{r} \rangle$ is maximized at $k^2 = 0$, further magnifying their contribution.
- Note, however, that in all three of these cases $|g_0|$ is either increased or decreased (compared with the idealized stellarator) for *all* localized particles although the relative differences are indeed largest at $k^2 = 0$. This result is perhaps somewhat surprising since it indicates that the reduction (increase) in the magnitude of f_0 due to drift optimization (amplification) is global and is not reversed near $k^2 = 1$ by the increase (reduction) in $\langle \dot{r} \rangle$ for shallowly trapped particles.
- HS5V10N once again offers a contrast; the g_0 curve indicates a very high degree of optimization with the relative improvement for more shallowly trapped particles at least the equal of that exhibited by ones which are deeply trapped. This is a unique property of Helias magnetic fields which fulfill the optimization principles laid out for Wendelstein 7-X [7].

Having a solution for f_0 also enables one to calculate analytical expressions for the fluxes and the diffusion coefficient in the so-called "ν^{-1} regime"

$$\begin{bmatrix} \Gamma \\ Q \end{bmatrix} = -\frac{\mathcal{A}_h}{m^{3/2}} \int d\kappa \begin{bmatrix} \kappa^{1/2} \\ \kappa^{3/2} \end{bmatrix} \frac{v_d^2}{\nu} \frac{\partial F_m}{\partial r} ,$$

$$D(\kappa) = \frac{\sqrt{2}}{8\pi} \frac{v_d^2}{\nu} \mathcal{A}_h ,$$

where

$$\mathcal{A}_h = \frac{64}{9} \frac{\epsilon_h^{3/2}}{\epsilon_t^2} \left\{ \mathcal{A}_0 - \frac{6}{5} \epsilon_h \mathcal{A}_1 + \frac{1621}{4200} \epsilon_h^2 \mathcal{A}_2 \right\}$$

$$\mathcal{A}_0 = C_{0,1}^2\left(1+\frac{3}{4}\sigma_2+\frac{3}{32}\sigma_1^2+\frac{3}{16}\sigma_2^2-\frac{3}{128}\sigma_2^3+\cdots\right)$$
$$+|C_{0,1}|C_{0,2}\left(3\sigma_1-\frac{1}{16}\sigma_1^3-\frac{3}{32}\sigma_1\sigma_2^2+\cdots\right)$$
$$+C_{0,2}^2\left(4+\frac{3}{4}\sigma_1^2+\frac{3}{8}\sigma_2^2+\frac{3}{32}\sigma_1^2\sigma_2+\cdots\right)$$

$$\mathcal{A}_1 = |C_{0,1}|\left(\sigma_1-\frac{3}{4}\sigma_1\sigma_2+\frac{3}{32}\sigma_1^3+\frac{3}{16}\sigma_1\sigma_2^2+\frac{1}{32}\sigma_1^3\sigma_2+\frac{3}{128}\sigma_1\sigma_2^3+\cdots\right)$$
$$-C_{0,2}\left(4\sigma_2-\frac{3}{2}\sigma_1^2+\frac{3}{4}\sigma_1^2\sigma_2+\frac{3}{8}\sigma_2^3+\frac{1}{32}\sigma_1^4+\frac{9}{64}\sigma_1^2\sigma_2^2+\cdots\right)$$

$$\mathcal{A}_2 = \sigma_1^2+4\sigma_2^2-\frac{9}{4}\sigma_1^2\sigma_2+\frac{3}{32}\sigma_1^4+\frac{15}{16}\sigma_1^2\sigma_2^2+\frac{3}{8}\sigma_2^4+\frac{1}{16}\sigma_1^4\sigma_2+\frac{21}{128}\sigma_1^2\sigma_2^3+\cdots .$$

Note that $\mathcal{A}_h$ is a purely geometrical quantity which contains all information concerning the magnetic field. To obtain these results, use has been made of

$$\int_0^1 dk^2\, K(k) = 2\,, \qquad \int_0^1 dk^2\, E(k) = \frac{4}{3}\,,$$

$$\int_0^1 dk^2\, k^2 K(k) = \frac{10}{9}\,, \qquad \int_0^1 dk^2\, k^2 E(k) = \frac{28}{45}\,,$$

$$\int_0^1 dk^2\, I(k^2)K(k) = \pi - \frac{56}{45}\,, \qquad \int_0^1 dk^2\, I(k^2)E(k) \approx \frac{2\pi}{3} - \frac{709}{700}\,.$$

The expressions for the fluxes can be shown to agree with those obtained by previous authors for more general magnetic fields [11,12].

Designing a stellarator magnetic field for reduced ν^{-1} transport is thus a matter of minimizing its geometrical factor, $\mathcal{A}_h$, to the greatest extent possible. In the lowest-order approximation, the smallest value possible occurs when

$$\frac{\sigma_1\epsilon_h}{|C_{0,1}|} = -\frac{\sigma_2\epsilon_h}{C_{0,2}} = \frac{2520}{1621}\,, \tag{11}$$

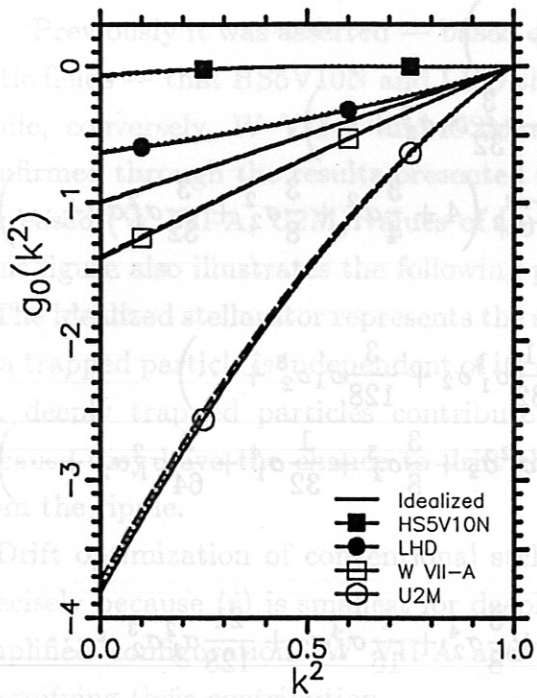

Figure 6. The poloidal average of the drift-weighted distribution function in the ν^{-1} regime, $g_0(k^2)$, is shown for an idealized stellarator, HS5V10N, LHD, W VII-A and U2M; results are for the $\rho = 0.5$ flux surface. The solid lines depict the analytic results given in the text while the equivalent power-series-solution curves are given by the broken lines (for $\xi = 1$) and the dotted lines (for $\xi = 0$).

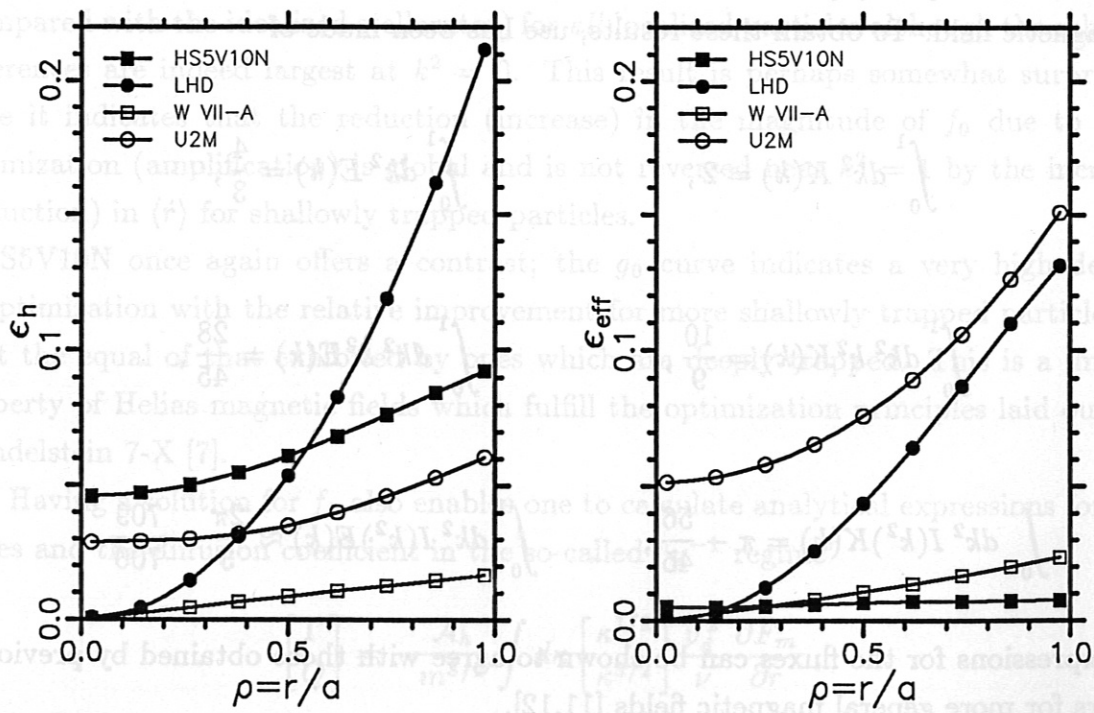

Figure 7. The radial dependence of the "effective" helical ripple for ν^{-1} transport, ϵ_{eff}, is plotted in the right-hand figure for the devices indicated. For comparison, the actual magnitude of the helical ripple, ϵ_h (as defined in Section II), is shown on the left. The effective helical ripple is defined so that $\epsilon_{eff} = \epsilon_h$ for the idealized model magnetic field.

and given that $C_{0,2}$ is $\mathcal{O}(\epsilon_t^2)$, the minimum value of the geometrical factor is found to be

$$\mathcal{A}_{h(\min)} \approx \frac{64}{9}\left(\frac{109}{1621}\right)\epsilon_h^{3/2}\left(\frac{C_{0,1}}{\epsilon_t}\right)^2 .$$

For classical stellarators and torsatrons, where $|C_{0,1}| \approx \epsilon_t$, it is therefore theoretically possible to reduce $\mathcal{A}_h$ by almost a factor of 15. In practice, however, the condition on σ_1 demanded by Equation (11) is difficult, if not impossible, to realize and one is forced to accept a lesser degree of optimization. In this regard, the Helias (with $|C_{0,1}| < \epsilon_t$) has a double advantage; not only is the condition on σ_1 much easier to fulfill but $\mathcal{A}_h$ is further reduced by the $(C_{0,1}/\epsilon_t)^2$ term, e.g. by an additional factor of six for HS5V10N.

The calculations presented in this section are perhaps best quantified by introducing the concept of the "effective" helical ripple for ν^{-1} transport,

$$\epsilon_{eff} = \left(\frac{9}{64}\mathcal{A}_h\right)^{2/3} .$$

When determining neoclassical losses in the ν^{-1} regime, it is then possible to treat any device as though it were an idealized stellarator with a helical ripple given by ϵ_{eff}. The radial dependence of this quantity for HS5V10N, LHD, W VII-A and U2M is given in Figure 7; for comparison, the magnitude of the actual helical ripple, ϵ_h, is also shown. The results illustrate how misleading the value of ϵ_h alone can be in predicting the level of ν^{-1} transport to be expected in a given configuration. The effective helical ripple is largest for U2M in spite of this device's modest values of ϵ_h; the counter-example is provided by HS5V10N where $\epsilon_{eff} < 0.01$ across the entire radial cross section. In the latter case ϵ_{eff} is a very weak function of the minor radius, indicating that the degree of drift optimization for HS5V10N steadily improves with increasing ρ.

To this point the calculations and results presented in this section have dealt only with the ν^{-1} regime. It has been shown that the Helias concept leads to extremely favorable neoclassical transport characteristics in this regime due, in part, to significant alterations in the perturbed distribution function which arise through drift optimization. Furthermore, these alterations in f have been confirmed by results from two different solutions of the bounce-averaged kinetic equation. The remainder of this section will be devoted to a relatively simple calculation of f for deeply trapped particles in the very-low collision frequency limit. Such particles make no contribution to the transport in this limit for the idealized stellarator [28] but, as will be shown, this is not the case for drift-optimized and drift-amplified configurations.

For $\nu_{eff} \ll \Omega_E$ the subsidiary ordering of the distribution function $f = f^0 + f^1 + \cdots$ is possible, where the superscript indicates the order of the small parameter $\hat{\nu} =$

ν_{eff}/Ω_E. Substituting into Equation (4) and solving for f^0, one obtains

$$f^0(\theta,k^2)=\frac{v_d}{\Omega_E\epsilon_t}\left\{\cos\theta\left(|C_{0,1}|-\sigma_1\epsilon_h\langle\cos\eta\rangle\right)-\cos 2\theta\left(C_{0,2}+\sigma_2\epsilon_h\langle\cos\eta\rangle\right)\right\}\frac{\partial F_m}{\partial r}\,.$$

(The integration constant has been dropped in this expression since it can be shown to be independent of both θ and k^2 and is therefore of no interest in the present calculation.) For deeply trapped particles it is possible to take $\langle\cos\eta\rangle=1-k^2-(k^2)^2/8$ and $A(k^2)/A'(k^2)=k^2$, and solve the kinetic equation in the next order,

$$f^1(\theta,k^2)=\frac{\hat\nu}{4}\frac{v_d}{\Omega_E}\frac{\epsilon_h}{\epsilon_t}(2+k^2)(2\sigma_1\sin\theta+\sigma_2\sin 2\theta)\frac{\partial F_m}{\partial r}\,,$$

where only the leading-order terms have been accounted for in the θ integration. The implications this result has for neoclassical transport rates may once again be illustrated by employing a (normalized) poloidal average of the drift-weighted distribution function

$$g^1(k^2)=\frac{1}{\hat\nu}\frac{\Omega_E}{v_d^2}\frac{1}{\pi}\int_0^{2\pi}d\theta\,\langle\dot r\rangle\,f^1\left(\frac{\epsilon_H}{\epsilon_h}\right)^{1/2}\left(\frac{\partial F_m}{\partial r}\right)^{-1}.$$

Again restricting the integration to leading-order terms, one finds for deeply trapped particles that

$$g^1(k^2)\approx\left(\frac{\epsilon_h}{\epsilon_t}\right)^2\left(1+\frac{k^2}{2}\right)\left\{\frac{\sigma_1|C_{0,1}|-\sigma_2C_{0,2}}{\epsilon_h}-(\sigma_1^{\,2}+\sigma_2^{\,2})(1-k^2)\right\}.$$

This result obviously confirms that of Reference [28]; for $\sigma_1=\sigma_2=0$ deeply trapped particles do not take part in the transport. One also observes that $g^1>0$ is a possibility, representing a *negative* contribution to the particle and heat fluxes; in other words, deeply trapped particles contribute to a *reduction* in the overall neoclassical transport. Roughly speaking, this occurs for stellarators with $0<\sigma_1<|C_{0,1}|/\epsilon_h$; LHD is an example of such a device. Conversely, $g^1<0$ for drift-amplified configurations ($\sigma_1<0$) such as W VII-A and U2M, so that deeply trapped particles serve to increase the neoclassical fluxes. This is also the case for HS5V10N which has $\sigma_1>|C_{0,1}|/\epsilon_h$.

This simple calculation of g^1 and the preceding comments concern only deeply trapped particles. It must be anticipated, however, that the transport associated with transition particles will be affected by drift optimization as well. Indeed, at first consideration one might expect negative consequences from the increase in $\langle\dot r\rangle$ which such particles experience in the ripple-trapped portions of their orbits. Actually, this turns out not to be the case; clarification of this apparent contradiction will be deferred at this point, however, and will instead be included in Section VI as part of a comprehensive look at the variation of the drift-weighted distribution function throughout the entire *lmfp* regime.

V. MONTE CARLO SIMULATIONS OF NEOCLASSICAL TRANSPORT

Numerical methods offer an additional means of investigating *lmfp* transport and can thereby provide an independent check on some aspects of the analytic theory. In this section the Monte Carlo technique is used to obtain estimates of the diffusion coefficient for each of the devices introduced in Section II and the results are compared with predictions of the analytic theory. A numerical approach also allows one to determine what effect additional harmonics — ignored by the analytic theory — have on the transport rates in the various configurations.

The Monte Carlo code used has been described previously [37] and will only briefly be summarized here. This numerical simulation is constructed so that particle orbits may be described either by a complete set of guiding-center equations (accurate regardless of the complexity of B) or through the iterative conservation of adiabatic invariants (which is much faster but accuracy suffers as the number of magnetic field harmonics increases). The complexity of the realistic stellarator fields considered here rules out this second option and the code was therefore run in a purely guiding-center mode. The magnetic field is specified through the Fourier expansion of B given in Equation (1), each device being characterized by its individual harmonics and their radial dependencies. This point bears repeating; the Monte Carlo simulation employs a general expression for B and not a simplified model magnetic field (such as that given in Equation (2)).

Parameters used in the Monte Carlo simulations are given in Table I. In all cases a stationary background plasma of either deuterons and electrons (D^+ , e^-) or protons and electrons (p^+ , e^-) has been assumed, with the species having equal densities and temperatures (i.e. $n_i = n_e = n$ and $T_i = T_e = T$). Monoenergetic electrons (with a

	HS5V10N	LHD	W VII-A	U2M
R_0, Major Radius (m)	5.5	3.9	2.0	1.7
a, Plasma Radius (m)	0.52	0.55	0.10	0.17
B_0, B on Axis (T)	2.5	3.0	3.0	2.0
p, Field Period Number	5	10	5	4
Test-Particle Energy (eV)	3000	3000	100	100
Plasma	D^+ , e^-	D^+ , e^-	p^+ , e^-	p^+ , e^-
T_i,T_e, Plasma Temp (eV)	3000	3000	100	100

Table I. Parameters used in the Monte Carlo simulations of neoclassical transport.

kinetic energy of eT) served as test particles in all simulations; electrons were chosen since they offer a much clearer separation of the *lmfp* regime from the "axisymmetric" (tokamak-like) results. Only pitch-angle scattering of the test particles was considered; the collision frequency was varied by changing the density of the background plasma. An electrostatic potential of the form $\Phi = \Phi_0(1-\rho^2)$ has been assumed and two cases have been investigated. First, the validity of the power-series solution throughout the entire *lmfp* regime was tested by setting $e\Phi_0 = 5T$; in a subsequent set of runs, $\Phi_0 = 0$ was chosen to facilitate a more detailed examination of the ν^{-1} regime. Each of these cases consisted of two subcases, one in which only magnetic-field harmonics with $m \leq 1$ were included in the Monte Carlo simulations, followed by a second in which all harmonics given in Figure 1 were present.

Results for the $\rho = 0.5$ flux surface in the case with $e\Phi_0 = 5T$ are presented in Figure 8 as plots of the diffusion coefficient as a function of the normalized collision frequency ν_{eff}/Ω_E. Monte Carlo estimates of D are shown by the blackened circles for simulations in which B was restricted to $m \leq 1$ harmonics, and by the open circles for simulations in which the full range of magnetic-field harmonics was accounted for. Power-series predictions of the trapped-particle contribution to D — obtained through numerical integration of Equation (9) — are given by the solid line for $\xi = 1$ and by the dotted line for $\xi = 0$. The broken line is the sum of the $\xi = 1$ curve and the expected "axisymmetric" contribution to D, given by the analytic fit

$$D_a = \left(D_{bp}^{3/2} + D_{PS}^{3/2}\right)^{2/3}$$

where $D_{bp} = D_b D_p/(D_b + D_p)$ and

$$D_b = \frac{|C_{0,1}|^{1/2}}{\epsilon_t^2}\frac{v_d R_0}{\Omega \iota^2}\nu \qquad D_p = \frac{2}{5}\left(\frac{C_{0,1}}{\epsilon_t}\right)^2 \frac{v_d v}{\Omega \iota} \qquad D_{PS} = \frac{7}{5}\left(\frac{C_{0,1}}{\epsilon_t}\right)^2 \frac{v_d R_0}{\Omega \iota^2}\nu$$

are the banana, plateau and Pfirsch-Schlüter diffusion coefficients, respectively, of standard axisymmetric neoclassical transport theory, modified to handle configurations for which $|C_{0,1}| \neq \epsilon_t$. In these expressions, $\Omega = qB/m$ is the gyrofrequency and ι is the rotational transform. The following points are worthy of notice:

- From a statistical point of view the two sets of Monte Carlo results are indistinguishable. Thus, for the four devices considered here, the analytic theory of neoclassical transport — in which only magnetic-field harmonics with $m \leq 1$ are considered — provides accurate predictions of the transport rates in the case where Ω_E is large.
- The results are insensitive to the value of ξ in the ν^{-1} regime and are only moderately affected at lower values of ν. The accuracy of the approximations used for the complete elliptic integrals is therefore not of critical concern.

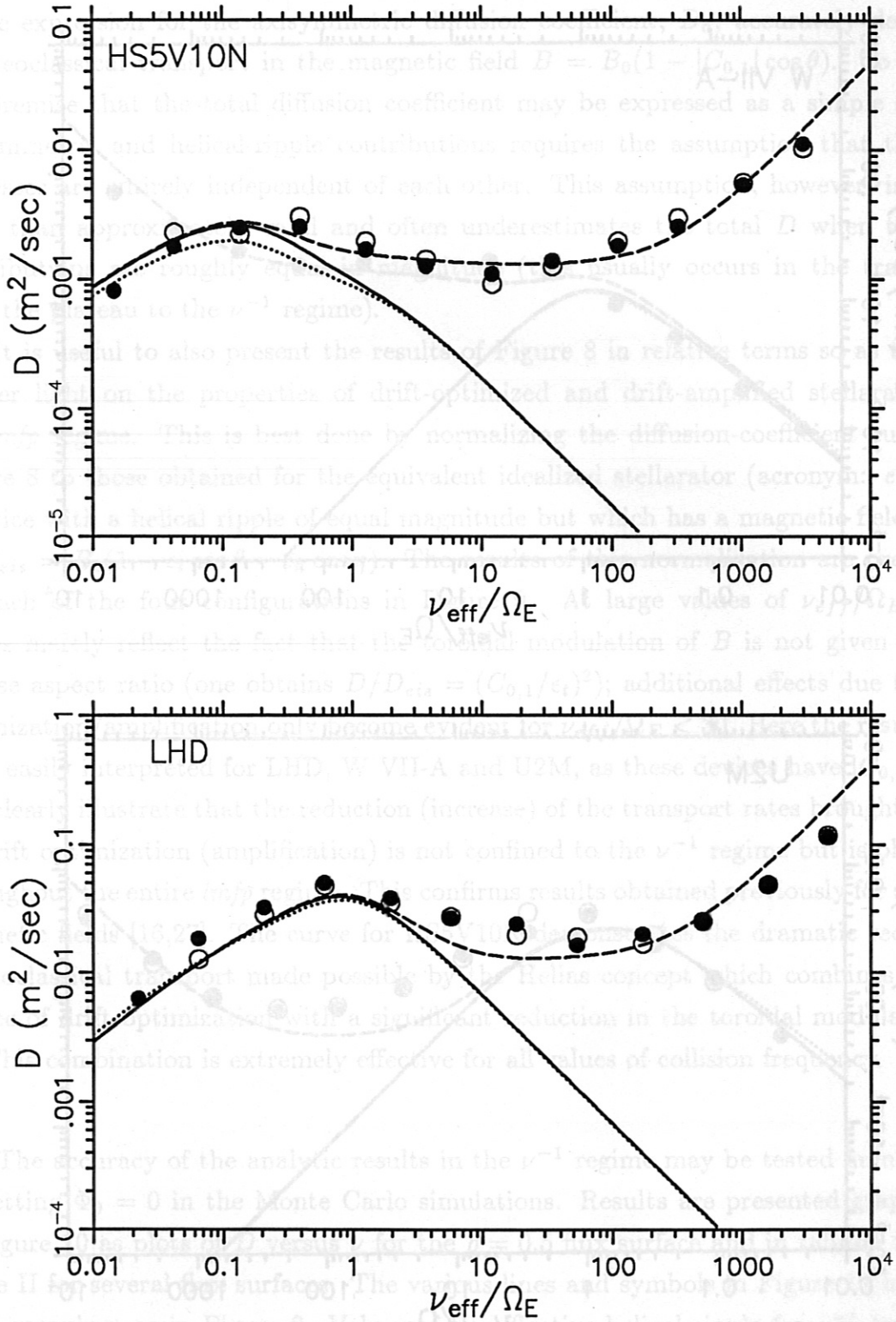

Figure 8. The diffusion coefficient is plotted as a function of normalized collision frequency for the $\rho = 0.5$ flux surface for HS5V10N, LHD, W VII-A and U2M. Power-series estimates of the trapped-particle contribution to D (from Equation (9)) are given by the solid line for $\xi = 1$ and by the dotted line for $\xi = 0$. The broken line is the sum of the $\xi = 1$ curve and an heuristic expression for the expected "axisymmetric" transport

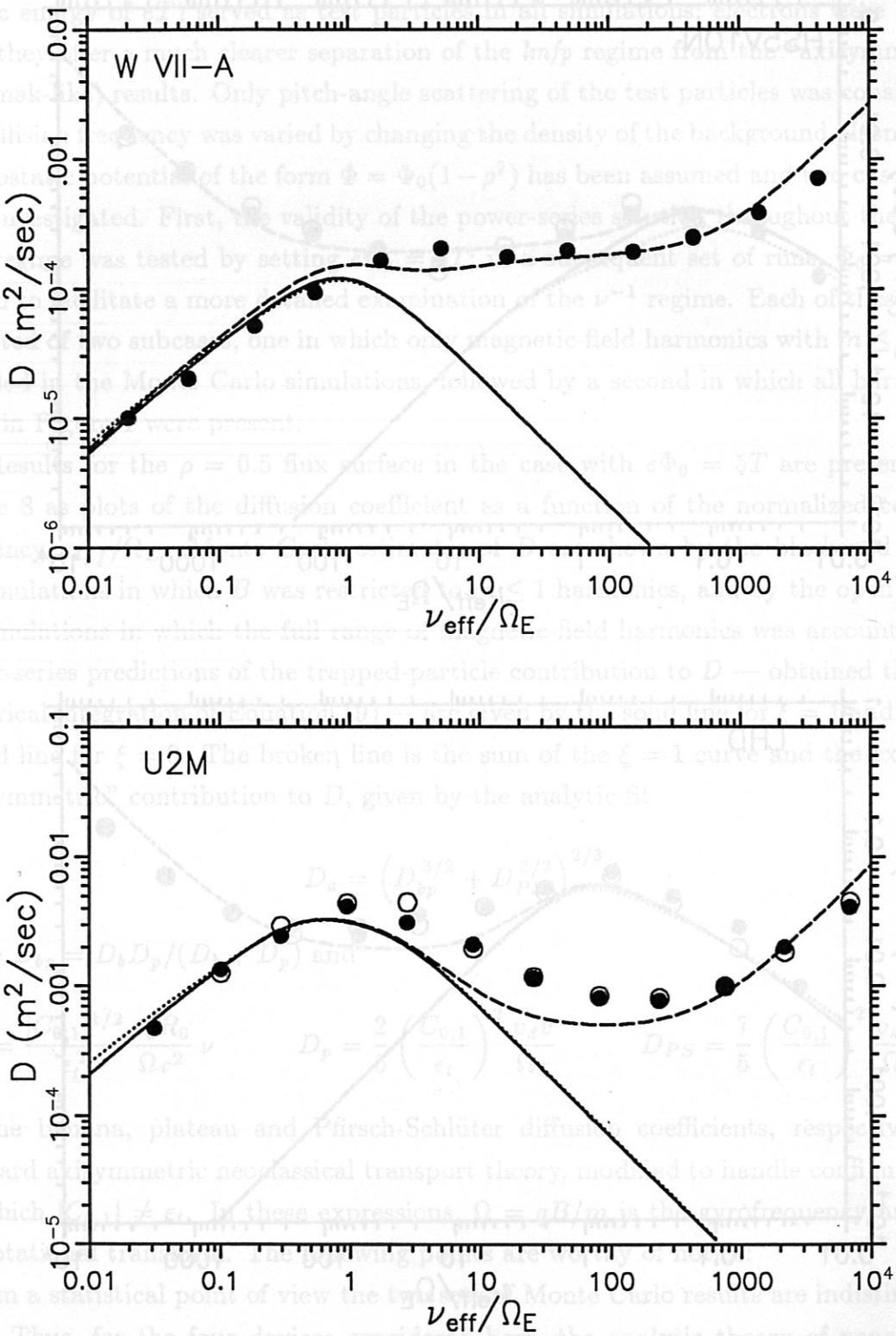

(given in the text). Results from Monte Carlo simulations in which the magnetic field was restricted to harmonics with $m \leq 1$ are given by the blackened circles; open circles depict the results which are obtained when the full range of magnetic-field harmonics is accounted for.

• The expression for the axisymmetric diffusion coefficient, D_a, accurately describes the neoclassical transport in the magnetic field $B = B_0(1 - |C_{0,1}| \cos\theta)$. To justify the premise that the total diffusion coefficient may be expressed as a simple sum of axisymmetric and helical-ripple contributions requires the assumption that the two processes are entirely independent of each other. This assumption, however, is never more than approximately valid and often underestimates the total D when the two contributions are roughly equal in magnitude (this usually occurs in the transition from the plateau to the ν^{-1} regime).

It is useful to also present the results of Figure 8 in relative terms so as to shed further light on the properties of drift-optimized and drift-amplified stellarators in the *lmfp* regime. This is best done by normalizing the diffusion-coefficient curves of Figure 8 to those obtained for the equivalent idealized stellarator (acronym: *eis*), i.e. a device with a helical ripple of equal magnitude but which has a magnetic field given by $B_{eis} = B_0(1 - \epsilon_t \cos\theta - \epsilon_h \cos\eta)$. The results of this normalization are presented for each of the four configurations in Figure 9. At large values of ν_{eff}/Ω_E these curves merely reflect the fact that the toroidal modulation of B is not given by the inverse aspect ratio (one obtains $D/D_{eis} = (C_{0,1}/\epsilon_t)^2$); additional effects due to drift optimization/amplification only become evident for $\nu_{eff}/\Omega_E < 30$. Here the results are most easily interpreted for LHD, W VII-A and U2M, as these devices have $|C_{0,1}| \approx \epsilon_t$, and clearly illustrate that the reduction (increase) of the transport rates brought about by drift optimization (amplification) is not confined to the ν^{-1} regime but is observed throughout the entire *lmfp* regime. This confirms results obtained previously for simpler magnetic fields [16,27]. The curve for HS5V10N demonstrates the dramatic reduction in neoclassical transport made possible by the Helias concept which combines a high degree of drift optimization with a significant reduction in the toroidal modulation of B. This combination is extremely effective for all values of collision frequency.

The accuracy of the analytic results in the ν^{-1} regime may be tested numerically by setting $\Phi_0 = 0$ in the Monte Carlo simulations. Results are presented graphically in Figure 10 as plots of D versus ν for the $\rho = 0.5$ flux surface and in tabular form in Table II for several flux surfaces. The various lines and symbols in Figure 10 have the same meanings as in Figure 8. Values of the effective helical ripple for ν^{-1} transport are determined from Monte Carlo estimates of the diffusion coefficient, D_{MC}, using the formula

$$\epsilon_{eff} = \left(\frac{9\sqrt{2}\pi}{16} \frac{\nu}{v_d^2} D_{MC} \right)^{2/3} .$$

Several comments may be made regarding these results.

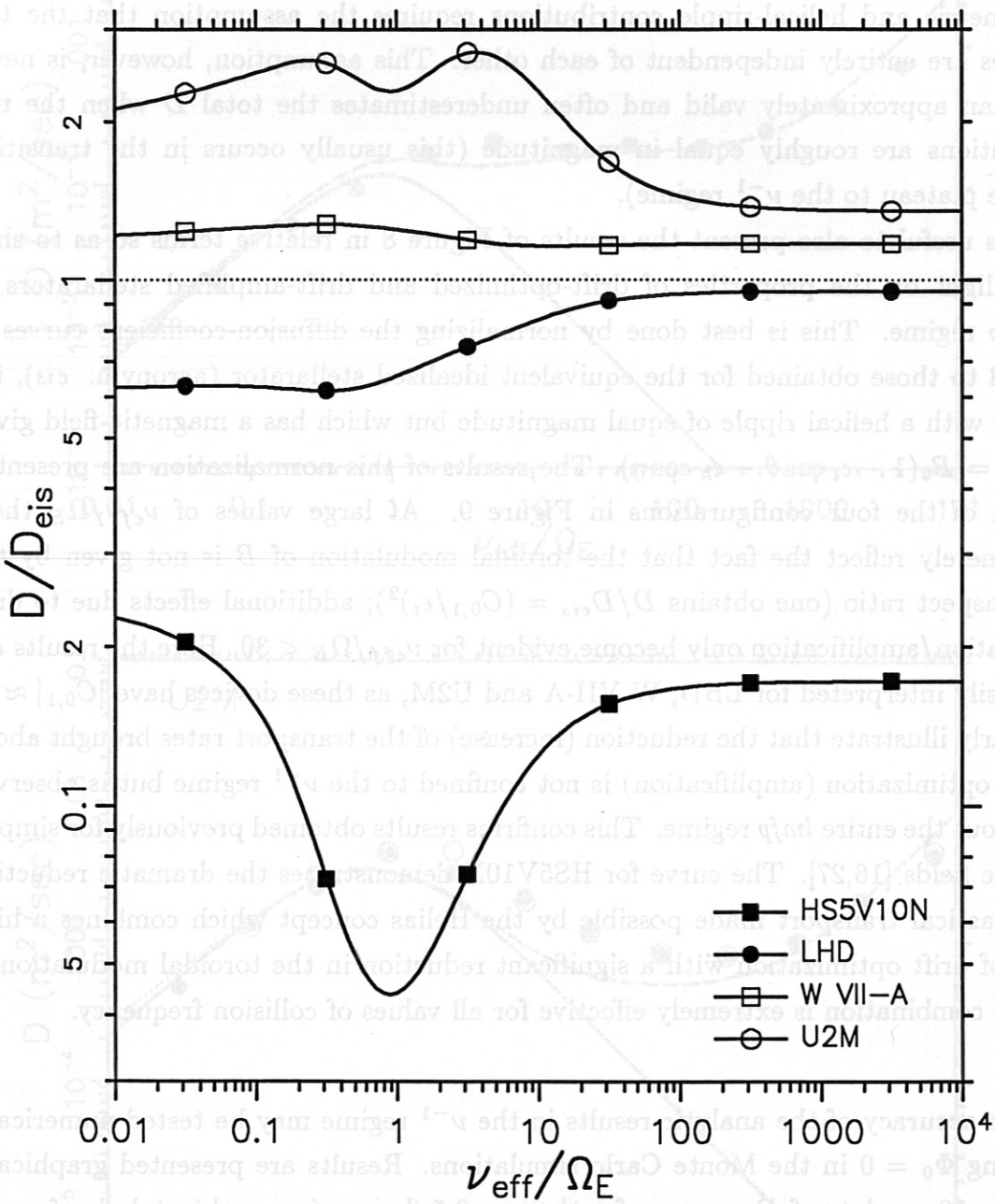

Figure 9. The diffusion coefficient, normalized to that of the equivalent idealized stellarator, is plotted as a function of normalized collision frequency for HS5V10N, LHD, W VII-A and U2M. Results are for the $\rho = 0.5$ flux surface with $e\Phi_0 = 5T$.

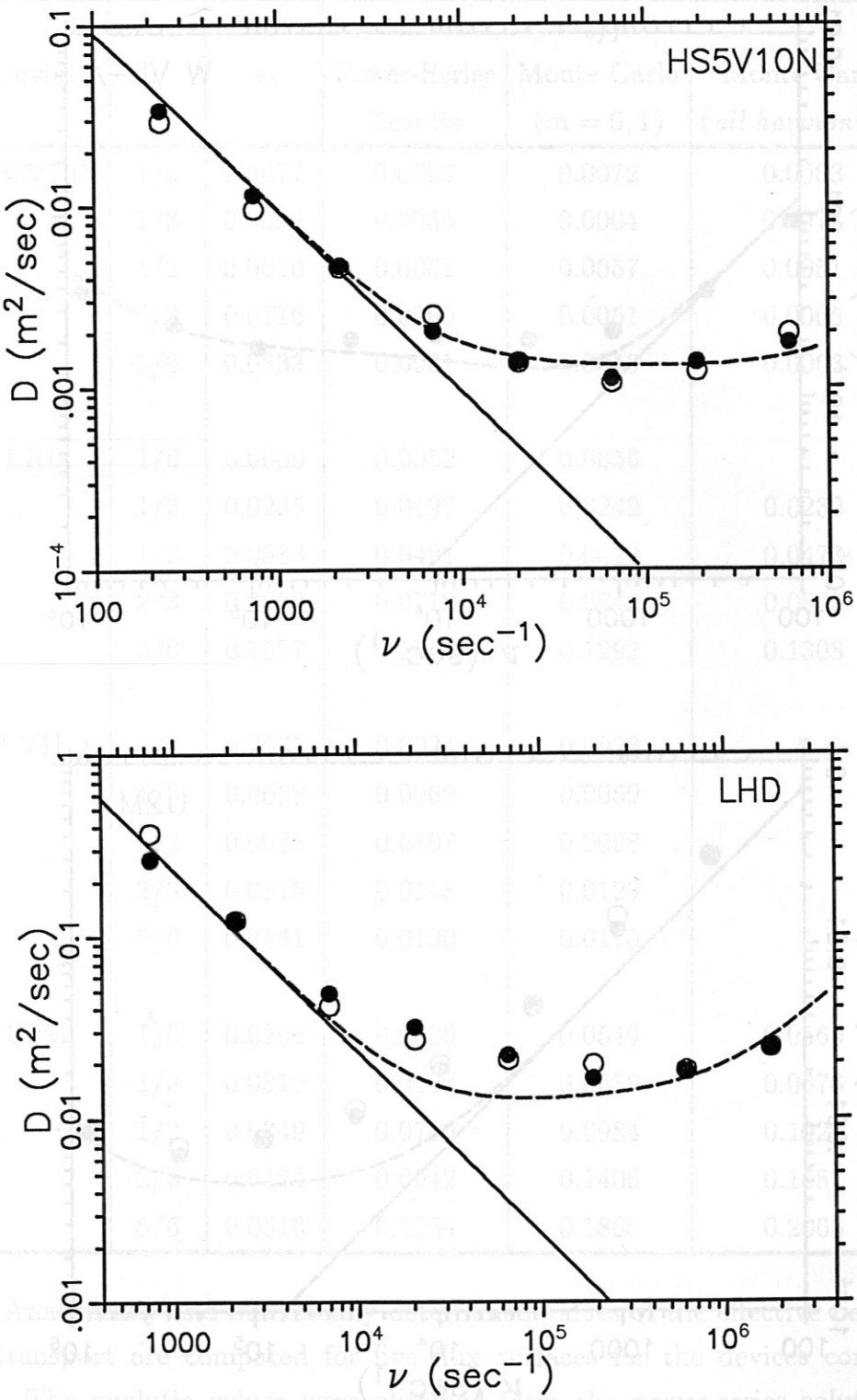

Figure 10. The diffusion coefficient is plotted as a function of collision frequency for the $\rho = 0.5$ flux surface for HS5V10N, LHD, W VII-A and U2M. The electrostatic potential has been set equal to zero; low-collision frequency simulations are thus in the ν^{-1} regime. Power-series estimates of the trapped-particle contribution to D (from Equation (9)) are given by the solid line (for $\xi = 1$). The broken line is the sum of the

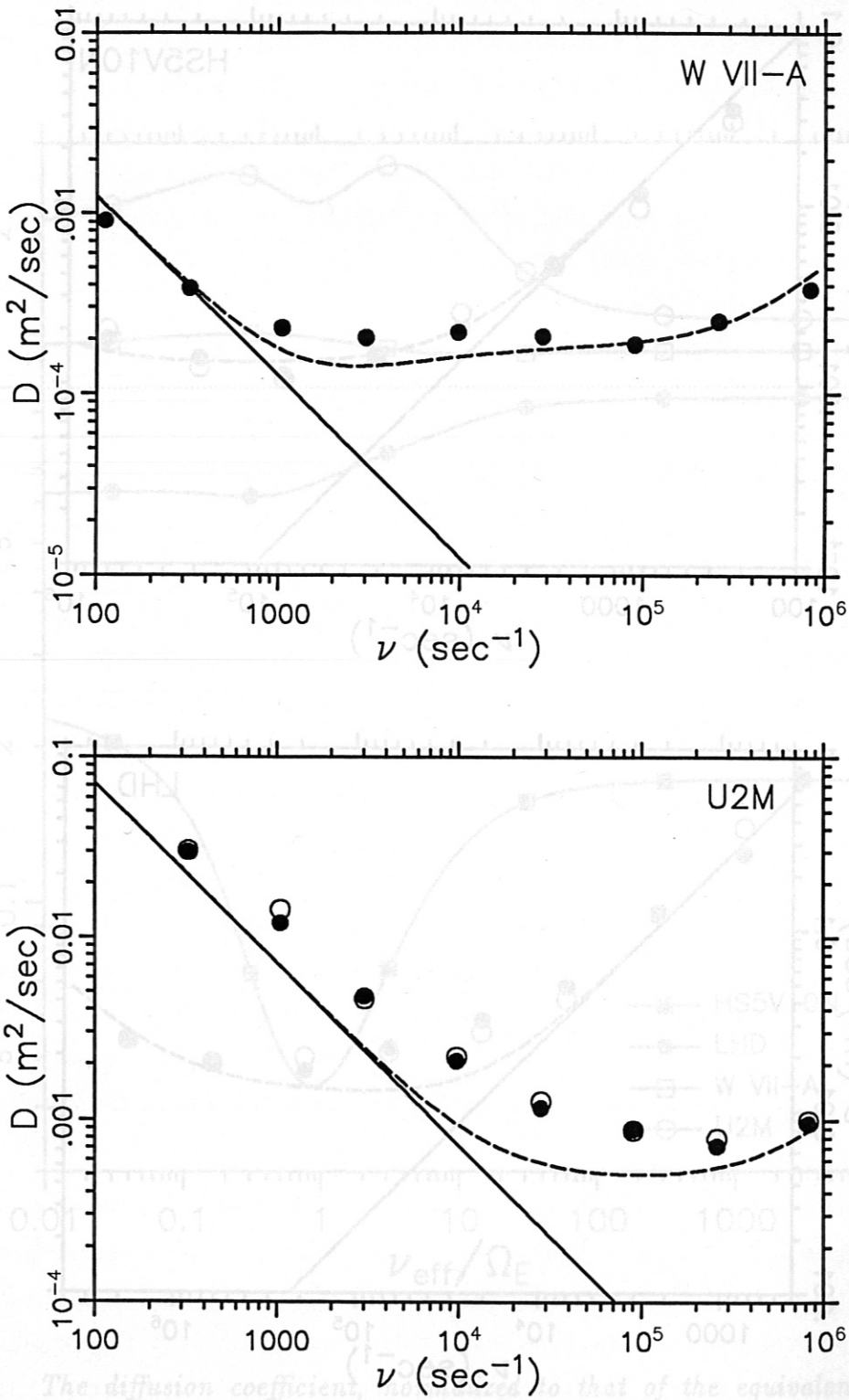

solid curve and an heuristic expression for the expected "axisymmetric" transport (given in the text). Results from Monte Carlo simulations in which the magnetic field was restricted to harmonics with $m \leq 1$ are given by the blackened circles; open circles depict the results which are obtained when the full range of magnetic-field harmonics is accounted for.

Device	ρ	ϵ_h	ϵ_{eff} Power-Series Results	ϵ_{eff} Monte Carlo ($m = 0, 1$)	ϵ_{eff} Monte Carlo (*all harmonics*)
HS5V10N	1/6	0.0477	0.0053	0.0072	0.0063
	1/3	0.0528	0.0056	0.0064	0.0074
	1/2	0.0610	0.0061	0.0057	0.0051
	2/3	0.0716	0.0065	0.0051	0.0065
	5/6	0.0833	0.0061	0.0043	0.0063
LHD	1/6	0.0060	0.0052	0.0056	*
	1/3	0.0235	0.0197	0.0242	0.0239
	1/2	0.0533	0.0421	0.0422	0.0473
	2/3	0.0962	0.0712	0.0844	0.0865
	5/6	0.1527	0.1054	0.1292	0.1308
W VII-A	1/6	0.0031	0.0034	0.0026	*
	1/3	0.0058	0.0069	0.0059	*
	1/2	0.0088	0.0108	0.0098	*
	2/3	0.0115	0.0148	0.0129	*
	5/6	0.0141	0.0190	0.0170	*
U2M	1/6	0.0292	0.0536	0.0549	0.0560
	1/3	0.0310	0.0609	0.0689	0.0678
	1/2	0.0349	0.0749	0.0984	0.1028
	2/3	0.0424	0.0942	0.1406	0.1687
	5/6	0.0516	0.1234	0.1866	0.2065

Table II. Analytically and numerically determined values of the effective helical ripple for ν^{-1} transport are compared for five flux surfaces for the devices considered in the text. The analytic values were obtained from the power-series solution of the bounce-averaged kinetic equation. Monte Carlo results are given in which the numerical simulations (a) were restricted to include only magnetic-field harmonics with $m \leq 1$, and (b) incorporated the full spectrum of B harmonics. An asterisk in the latter column indicates that the magnetic fields of cases (a) and (b) are identical.

• A shortcoming of the analytic theory presented here is the neglect of some of the effects which non-localized particles have on the diffusion coefficient. This neglect is embodied in the zero-banana-width approximation and in the boundary conditions $Y(1) = W(1) = 0$ (the boundary conditions on the even part of f, however, do account for the effects of transition particles). As a consequence, the analytic results generally underestimate D at the onset of the ν^{-1} regime, an effect which has been alluded to previously. This behavior is clearly exhibited in the frames of Figure 10 although its degree varies from configuration to configuration (a result which has also been observed in [26]). To address this problem, numerical solutions of the full ripple-averaged kinetic equation have been developed [27,32,34]. These have the drawback, however, of requiring much more computer time (factors of between 10^4 and 10^6) than the power-series solution described here in Section III.

• For HS5V10N and W VII-A, the relative statistical errors for the Monte Carlo values of D satisfy $\sigma/(D_{MC}\sqrt{N}) \lesssim 0.3$ (where σ is the standard deviation and N the number of test particles). These configurations have small values of ϵ_{eff} so that the ν^{-1} scaling of the diffusion coefficient first appears at rather low values of ν; finite computer resources force one to consider these cases with small numbers of test particles. For LHD and U2M simulations one obtains $\sigma/(D_{MC}\sqrt{N}) \lesssim 0.2$.

• In a comparison of the power-series and Monte Carlo results (for $m \leq 1$), one finds for the inner flux surfaces ($\rho \leq 0.5$) that the analytically determined value of D is usually to be found in the interval $D_{MC} - \sigma/\sqrt{N} < D < D_{MC} + \sigma/\sqrt{N}$. The analytical and numerical results agree less well for the outer flux surfaces. In particular, for U2M, the Monte Carlo estimates of ϵ_{eff} are considerably larger than the analytic values.

• Including higher-order magnetic-field harmonics in the Monte Carlo simulations has no statistically significant effect on the diffusion coefficient for the inner flux surfaces. A modest degradation in confinement is observed, however, for the outer flux surfaces of HS5V10N and U2M.

• The favorable transport characteristics of HS5V10N, predicted by analytic calculations based on a model magnetic field, are confirmed by Monte Carlo simulations which account for the full complexity of B. In particular, the result $\epsilon_{eff}(r) < 0.01$ is verified.

VI. OBSERVATIONS AND CONCLUSIONS

In Section IV, two poloidal averages of the drift-weighted distribution function were introduced and used to investigate the behavior of deeply trapped particles in the limits $\hat{\nu} \gg 1$ and $\hat{\nu} \ll 1$. By employing a generalized form of these averages it is possible to explain what is perhaps the most interesting aspect of the results depicted in Figure 8, namely that for HS5V10N, the maximum value of the diffusion coefficient in the *lmfp* regime does not occur for $\hat{\nu} \approx 1$ (as it does for the other three devices), but is instead shifted to a considerably lower value of collision frequency.

It is easy to verify that

$$g(k^2) = \max\left\{\hat{\nu}, \hat{\nu}^{-1}\right\} \frac{\Omega_E}{v_d^2} \frac{1}{\pi} \int_0^{2\pi} d\theta \, \langle \dot{r} \rangle \, f \left(\frac{\epsilon_H}{\epsilon_h}\right)^{1/2} \left(\frac{\partial F_m}{\partial r}\right)^{-1}$$

reduces to the expressions for $g_0(k^2)$ and $g^1(k^2)$ in the appropriate limits and is continuous at $\hat{\nu} = 1$. In what follows, however, it will prove more instructive to use a slightly modified version of $g(k^2)$, denoted by

$$\hat{g}(k^2) = \frac{g(k^2)}{\max\left\{\hat{\nu}, \hat{\nu}^{-1}\right\}}.$$

Plots of this latter quantity not only reveal which portions of the trapped-particle population are important to the diffusive process, they also represent a normalized measure of its magnitude.

First consider an idealized stellarator magnetic field. For large values of collision frequency the ν^{-1} result $\hat{g} = (k^2 - 1)\hat{\nu}^{-1}$ is obtained. As was pointed out previously, this result clearly shows that deeply trapped particles are mainly responsible for ν^{-1} transport, drifting furthest off of their original flux surface before being collisionally removed from the local ripple. The radial excursions of trapped particles are thus limited by collisions and this remains true until the effective collision frequency, ν_{eff}, becomes small enough that such particles have the chance to complete a significant portion of a poloidal transit before being collisionally detrapped. At this point the radial excursion is limited *collisionlessly* by the poloidal precession frequency, Ω_E, signifying the end of the ν^{-1} regime. The most deeply trapped particles are the first to experience the beneficial effects of Ω_E and there exists a transitionary range of collision frequencies in which shallowly trapped particles continue to exhibit ν^{-1} behavior while the contribution to $\hat{g}(k^2)$ from the deeply trapped particles begins to decline. The transport coefficients attain their maximum value for $\nu_{eff} \approx \Omega_E$ and then decrease with decreasing collision frequency as the contribution made by deeply trapped particles falls rapidly, more than offsetting the enhancement experienced by particles which are more shallowly trapped.

Since the trapped-particle trajectories are independent of k^2, the contribution that deeply trapped particles make to $\hat{g}(k^2)$ must ultimately fall to zero in the limit $\hat{\nu} \ll 1$, as was shown in Section IV.

This evolution of $\hat{g}(k^2)$ with collision frequency is illustrated in the top frame of Figure 11 with results obtained from the power-series solution of the bounce-averaged kinetic equation (for $\xi = 1$). Parameters for this idealized stellarator have been chosen to facilitate a direct comparison with the $\rho = 0.5$ flux surface of LHD. This figure clearly illustrates the progression of $\hat{g}(k^2)$ from the ν^{-1} regime (represented here by the $\hat{\nu} = 3$ curve) into transition ($\nu_{eff} = \Omega_E$), after which the contribution of the deeply trapped particles rapidly diminishes ($\hat{\nu} = 0.3$ and $\hat{\nu} = 0.1$) and finally goes to zero ($\hat{\nu} = 0.03$).

This process is repeated in the lower frame of Figure 11 for the actual LHD parameters at $\rho = 0.5$. Although the relative contribution of the deeply trapped particles has been reduced, these particles nevertheless continue to dominate the transport for $\hat{\nu} \gtrsim 1$ and the evolution of $\hat{g}(k^2)$ with collision frequency is qualitatively the same as that of the idealized stellarator. When $\hat{\nu}$ becomes small the deeply trapped particles do indeed make a positive contribution to $\hat{g}(k^2)$ (as predicted in Section IV) but this effect is a minor one when compared to the reduction in the magnitude of $\hat{g}(k^2)$ experienced by the shallowly trapped particles.

In the case of HS5V10N, it is instructive to begin by considering a "simplified" version of the device which retains its actual values of $C_{0,1}$ and ϵ_h but for which the drift optimization has been "removed" (by setting $\sigma_1 = \sigma_2 = 0$). Such a configuration illustrates the consequences which reduction of the toroidal modulation of B has, by itself, on the neoclassical transport rates; the results are plotted in the upper frame of Figure 12. Qualitatively, the $\hat{g}(k^2)$ curves are again the same as those found for the idealized stellarator. Quantitatively, the magnitude of each curve has been reduced by a factor of $(|C_{0,1}|/\epsilon_t)^\alpha$, where $\alpha = 2$ in the ν^{-1} regime and then decreases slowly in value with decreasing collision frequency, tending toward $\alpha = 1$ as $\hat{\nu} \to 0$.

The high degree of drift optimization present for the actual parameters of HS5V10N leads to a quite different evolution of the $\hat{g}(k^2)$ curves, however, as can be seen in the lower frame of Figure 12. Here, $\langle \dot{r} \rangle \approx 0$ for a range of k^2 values, thereby guaranteeing that particles in a particular region of phase space are unimportant to the transport process, regardless of the value of $\hat{\nu}$. In the current example this occurs near $k^2 = 0.4$, i.e. for particles which would otherwise be among the first to be affected by the $\mathbf{E} \times \mathbf{B}$ precession frequency for $\hat{\nu} \lesssim 1$. As a consequence, the beneficial influence of Ω_E on the neoclassical transport rates is "postponed" for HS5V10N. Instead of peaking shortly after the end of the ν^{-1} regime ($\nu_{eff} \approx \Omega_E$), the diffusion coefficient continues to increase with decreasing collision frequency, finally reaching its maximum value for

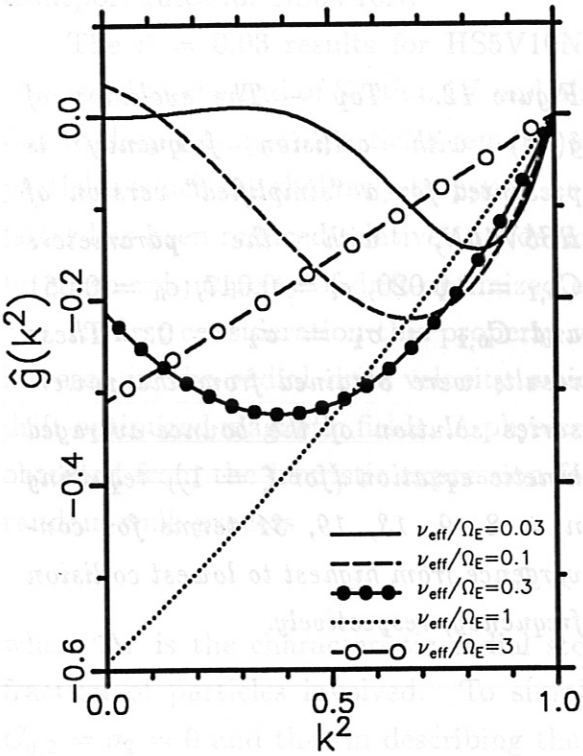

Figure 11. Top— The evolution of $\hat{g}(k^2)$ *with collision frequency is presented for an idealized stellarator (LHD-like) with the parameters* $|C_{0,1}| = \epsilon_t = 0.071$, $\epsilon_h = 0.053$ *and* $\sigma_1 = \sigma_2 = 0$. *These results were obtained from the power-series solution of the bounce-averaged kinetic equation (for* $\xi = 1$*), requiring* $n = 8$, *9, 13, 19, 30 terms for convergence from highest to lowest collision frequency, respectively.*

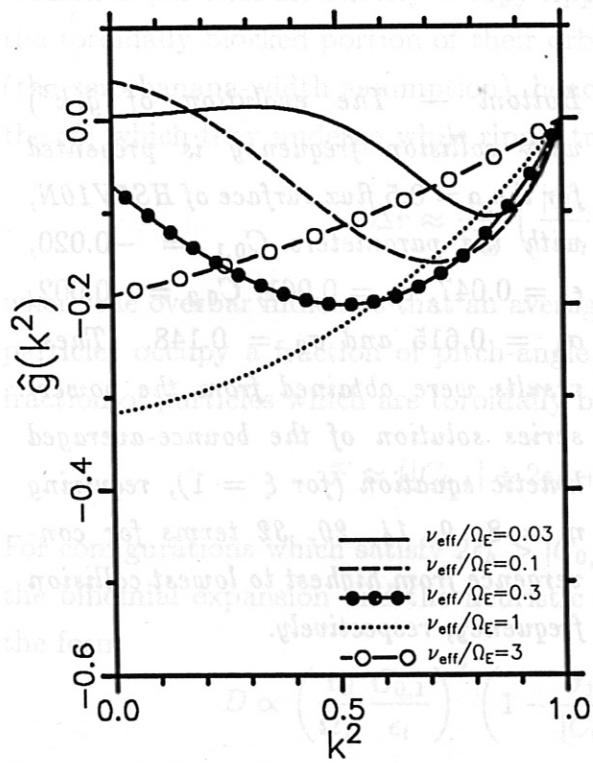

Bottom — The evolution of $\hat{g}(k^2)$ *with collision frequency is presented for the* $\rho = 0.5$ *flux surface of LHD, with the parameters* $C_{0,1} = -0.069$, $\epsilon_t = 0.071$, $\epsilon_h = 0.053$, $\sigma_1 = 0.315$ *and* $\sigma_2 = 0.040$. *These results were obtained from the power-series solution of the bounce-averaged kinetic equation (for* $\xi = 1$*), requiring* $n = 8$, *9, 13, 19, 30 terms for convergence from highest to lowest collision frequency, respectively.*

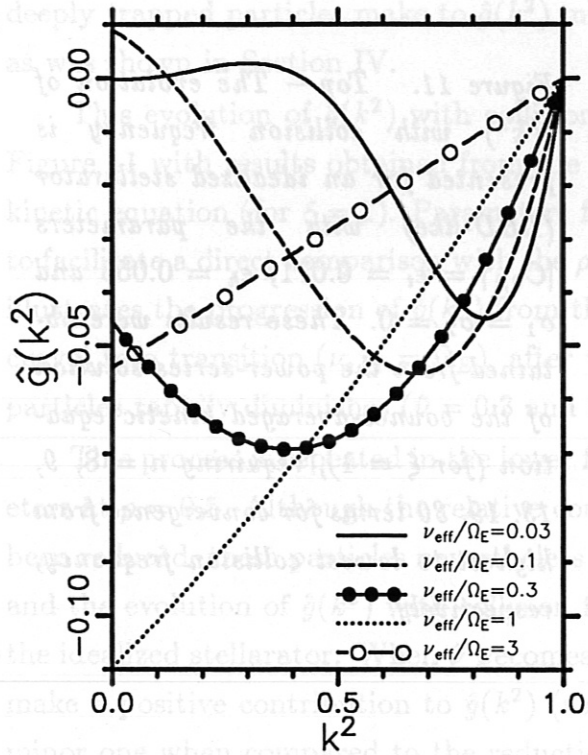

Figure 12. Top — The evolution of $\hat{g}(k^2)$ *with collision frequency is presented for a "simplified" version of HS5V10N, with the parameters* $C_{0,1} = -0.020$, $\epsilon_t = 0.047$, $\epsilon_h = 0.061$ *and* $C_{0,2} = \sigma_1 = \sigma_2 = 0$. *These results were obtained from the power-series solution of the bounce-averaged kinetic equation (for* $\xi = 1$*), requiring* $n = 8$, *9, 13, 19, 31 terms for convergence from highest to lowest collision frequency, respectively.*

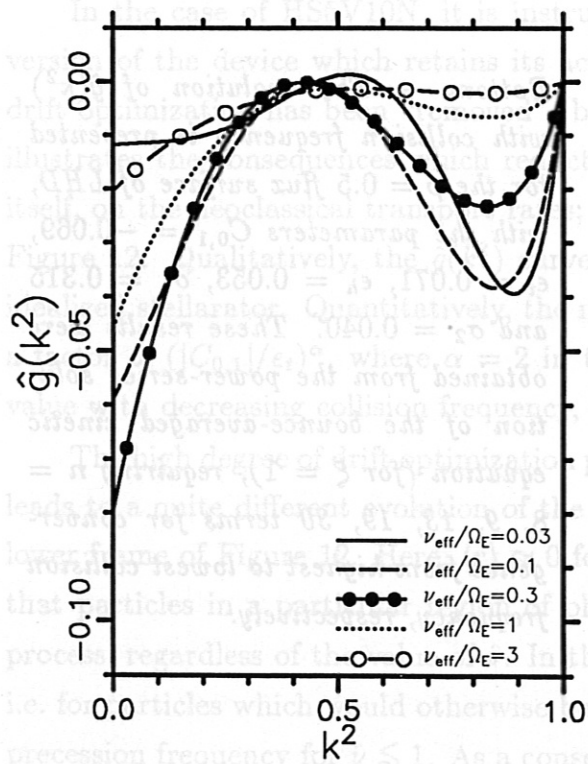

Bottom — The evolution of $\hat{g}(k^2)$ *with collision frequency is presented for the* $\rho = 0.5$ *flux surface of HS5V10N, with the parameters* $C_{0,1} = -0.020$, $\epsilon_t = 0.047$, $\epsilon_h = 0.061$, $C_{0,2} = -0.002$, $\sigma_1 = 0.615$ *and* $\sigma_2 = 0.148$. *These results were obtained from the power-series solution of the bounce-averaged kinetic equation (for* $\xi = 1$*), requiring* $n = 8$, *9, 14, 20, 32 terms for convergence from highest to lowest collision frequency, respectively.*

$\hat{\nu} \approx 0.1$; only at this point is Ω_E finally successful in effecting a reduction in the transport rates for HS5V10N.

The $\hat{\nu} = 0.03$ results for HS5V10N are further confirmation of the calculation presented at the end of Section IV and also provide an example in which the transport due to deeply trapped particles remains an appreciable fraction of that attributable to particles which are shallowly trapped. As in the case of LHD, transport ascribed to the latter has been reduced relative to a device with $\sigma_1 = \sigma_2 = 0$, suggesting that this may be a general property of drift-optimized configurations.

At first consideration this property would seem to be rather surprising, given the increase in the radial drift velocity which shallowly trapped particles experience in drift-optimized magnetic fields. A physical explanation of this seeming paradox may be obtained from the heuristic expression for the diffusion coefficient due to a collisional random-walk process

$$D \propto \frac{(\Delta r)^2}{\mathcal{F}} \nu ,$$

where Δr is the characteristic radial step size of the diffusive process and $\mathcal{F}$ is the fraction of particles involved. To simplify the calculation it will be assumed that $C_{0,2} = \sigma_2 = 0$ and that in describing the transport due to shallowly trapped particles for $\hat{\nu} \ll 1$ it is sufficient to consider the behavior of transition particles. (Recall that transition particles alternately occupy ripple-trapped and toroidally blocked states.) In the toroidally blocked portion of their orbits, these particles experience no radial drift (the zero-banana-width assumption), hence their diffusive radial step is determined by the $\langle \dot{r} \rangle$ which they undergo while ripple trapped and is given by

$$\Delta r \approx \frac{v_d}{\Omega_E} \left(\frac{|C_{0,1}|}{\epsilon_t} - \frac{\sigma_1 \epsilon_h}{\epsilon_t} \overline{\langle \cos \eta \rangle} \right)$$

where the overbar indicates that an average value of $\langle \cos \eta \rangle$ has been taken. Transition particles occupy a fraction of pitch-angle space which is approximately given by the fraction of particles which are toroidally blocked [38], i.e.

$$\mathcal{F} \approx \left(|C_{0,1}| + 2\epsilon_h + \sigma_1 \epsilon_h \right)^{1/2} - \left(2\epsilon_h \right)^{1/2} .$$

For configurations which satisfy $2\epsilon_h > |C_{0,1}| + \sigma_1 \epsilon_h$, this result may be simplified using the binomial expansion and the heuristic expression for the diffusion coefficient takes the form

$$D \propto \left(\frac{v_d}{\Omega_E} \frac{C_{0,1}}{\epsilon_t} \right)^2 \left(1 - \frac{\sigma_1 \epsilon_h}{|C_{0,1}|} \overline{\langle \cos \eta \rangle} \right)^2 \frac{\epsilon_h^{1/2} \nu}{(|C_{0,1}| + \sigma_1 \epsilon_h)} .$$

For $\sigma_1 = 0$ this reduces to the usual ν-regime result [28,38,39]

$$D \propto \left(\frac{v_d}{\Omega_E} \right)^2 \frac{|C_{0,1}| \, \epsilon_h^{1/2} \nu}{\epsilon_t^2} .$$

It is then straightforward to show that drift optimization leads to a reduction in ν-regime transport if the average value of $\langle \cos\eta \rangle$ satisfies

$$\langle \overline{\cos\eta} \rangle > \frac{|C_{0,1}|}{\sigma_1 \epsilon_h} \left\{ 1 - \left(1 + \frac{\sigma_1 \epsilon_h}{|C_{0,1}|} \right)^{1/2} \right\}.$$

For drift-amplified devices the sense of the inequality must be reversed and one can show that $\langle \overline{\cos\eta} \rangle < -0.5$ is necessary to effect a reduction in the ν-regime transport due to transition particles. Referring to Figure 3, one sees that this condition is impossible to fulfill; coupled with the additional losses attributable to deeply trapped particles (demonstrated at the end of Section IV) it is clear that a drift-amplified stellarator must have larger ν-regime transport rates than a comparable idealized device. This observation is supported by the very-low-ν results for W VII-A and U2M given in Figure 9.

For the drift-optimized examples considered in Figures 11 and 12 the inequality requires that for LHD, $\langle \overline{\cos\eta} \rangle > -0.473$, and for HS5V10N, $\langle \overline{\cos\eta} \rangle > -0.371$. The variation in k^2 which a transition particle undergoes in the ripple-trapped portion of its orbit may be estimated from [27]

$$\Delta k^2 = \frac{|\dot{k}^2|}{\Omega_E} \approx \frac{\sigma_1}{4} + \frac{v_d}{\Omega_E} \frac{|C_{0,1}|}{\epsilon_t} \frac{1}{4\epsilon_h} \frac{\partial \epsilon_h}{\partial r}.$$

Again referring to Figure 3, one sees that a variation of this magnitude is more than sufficient to insure that the inequalities are satisfied. These two examples provide illustration of a general result: the favorable neoclassical transport characteristics of drift-optimized stellarators are not confined to the ν^{-1} regime, but extend throughout the entire *lmfp* regime.

As a final observation, it should be commented that all specific calculations presented in this paper were for vacuum fields and for the "standard" configurations of the devices being considered. Modified configurations — whether the modifications are due to finite plasma pressure or alterations in the currents carried by the magnetic-field coils — may be handled equally as well. All that is required is a knowledge of the modified B in flux coordinates and that it be possible to accurately approximate this magnetic field using the model for B given in Equation (2).

In conclusion, solutions of the bounce-averaged kinetic equation have been presented which may be used to determine the neoclassical transport in stellarator-type devices caused by the presence of localized particles, i.e. those trapped in the helical ripples of the stellarator's magnetic field. The most general of these solutions is valid for the full range of collision frequencies which constitute the *long-mean-free-path* regime.

The remaining solutions are appropriate only for a particular ordering of the kinetic equation (being asymptotically valid in the limit of a small expansion parameter) but provide important physical insights. All calculations assume a model magnetic field which is an accurate approximation to the actual B for a wide variety of stellarator-type devices, including Helias configurations as well as conventional stellarators and torsatrons.

The solutions of the kinetic equation have been used to investigate the neoclassical transport properties of the Helias HS5V10N (the reference configuration for Wendelstein 7-X), as well as those of LHD, W VII-A and U2M. These four configurations also allow one to examine the features of neoclassical transport in drift-optimized (HS5V10N and LHD) and drift-amplified (W VII-A and U2M) stellarators, using actual magnetic fields. It has been confirmed that drift-optimized devices exhibit improved neoclassical confinement throughout the entire *lmfp* regime; conversely, drift amplification results in universal degradation of the confinement. It has also been demonstrated that the Helias concept leads to large reductions in neoclassical transport rates relative to the levels typical in conventional stellarators and torsatrons. This reduction is particularly dramatic in the ν^{-1} regime — the losses in HS5V10N are comparable to those of a conventional stellarator with $\epsilon_h \lesssim 0.01$ — but is significant for all other values of collision frequency as well. Further, the high degree of drift optimization in Helias alters the role deeply trapped particles play in the transport process; as a consequence, the transport coefficients reach their maximum values at lower values of collision frequency than is usual.

These results have been confirmed numerically with Monte Carlo simulations. In most of the cases investigated, particle diffusion coefficients determined analytically agree well with the statistical estimates obtained numerically. The discrepancies in the remaining cases are in all likelihood a consequence of the simplified manner in which non-localized particles have been treated in the solutions of the kinetic equation. Work is currently underway to alleviate this shortcoming by solving the full ripple-averaged kinetic equation, i.e. by solving simultaneously the appropriate kinetic equations for localized and non-localized particles.

ACKNOWLEDGEMENT

The work of Dr. Hitchon was supported by U.S. Department of Energy Grant No. DE-FG02-85ER53201.

REFERENCES

[1] Brossmann U, Dommaschk W, Herrnegger F, Grieger G, Kisslinger J, Lotz W, Nührenberg J, Rau F, Renner H, Ringler H, Sapper J, Schlüter A and Wobig H, 1983 **Plasma Physics and Controlled Nuclear Fusion Research, Proc. 9th Int. Conf. (Baltimore MD, USA, 1982)**, Vol. 3 (Vienna: IAEA) p 141

[2] Nührenberg J and Zille R, 1986 **Phys. Lett. A 114**, 129

[3] Dommaschk W, Herrnegger F, Lotz W, Merkel P, Nührenberg J, Schlüter A, Schwenn U and Zille R, 1987 **Plasma Physics and Controlled Nuclear Fusion Research, Proc. 11th Int. Conf. (Kyoto, Japan, 1986)**, Vol. 2 (Vienna: IAEA) p 383

[4] Nührenberg J and Zille R, 1988 **Phys. Lett. A 129**, 113

[5] Merkel P, 1987 **Nucl. Fusion 27**, 867

[6] Kisslinger J, 1988 **Proceedings of the Second Workshop on Wendelstein VII-X (Schloss Ringberg, Germany, 13-16 June 1988), Rau F and Leotta G G, Editors**, (Commission of the European Communities, EUR 11705 EN) p 245

[7] Beidler C D, Grieger G, Herrnegger F, Harmeyer E, Kisslinger J, Lotz W, Maassberg H, Merkel P, Nührenberg J, Rau F, Sapper J, Sardei F, Scardovelli R, Schlüter A and Wobig H, 1990 **Fusion Technol. 17**, 148

[8] Wobig H, 1987 **Proceedings of the Workshop on Wendelstein VII-X (Schloss Ringberg, Germany, 18-20 March 1987), Rau F and Leotta G G, Editors**, (Commission of the European Communities, EUR 11058 EN) p 93

[9] Rodriguez-Solano Ribeiro E and Shaing K C, 1987 **Phys. Fluids 30**, 462

[10] Mynick H E, Chu T K and Boozer A H, 1982 **Phys. Rev. Lett. 48**, 322

[11] Shaing K C and Hokin S A, 1983 **Phys. Fluids 26**, 2136

[12] Kovrizhnykh L M, 1984 **Nucl. Fusion 24**, 851

[13] Bykov V E, Georgievskij A V, Peletminskaya V G, Khodyachikh A V and Shishkin A A, 1984 **Nucl. Fusion 24**, 1195

[14] Lotz W and Nührenberg J, 1988 **Phys. Fluids 31**, 2984

[15] Lotz W, 1988 **Proceedings of the Second Workshop on Wendelstein VII-X (Schloss Ringberg, Germany, 13-16 June 1988), Rau F and Leotta G G, Editors**, (Commission of the European Communities, EUR 11705 EN) p 97

[16] Beidler C D, Hitchon W N G, van Rij W I, Hirshman S P and Shohet J L, 1987 **Phys. Rev. Lett. 58**, 1745

[17] D'haeseleer W D, Hitchon W N G, Callen J D and Shohet J L, 1991 **Flux Coordinates and Magnetic Field Structure**, (Springer, New York)

[18] Iiyoshi A, Fujiwara M, Motojima O, Ohyabu N and Yamazaki K, 1990 **Fusion Technol. 17**, 169

[19] Blaumoser M, Freudenberger K, Grieger G, Jaenicke R, Junker J, Knobloch A, Kolos J, Kunze R C, Lohnert H, Oswald B, Pöhlchen R, Streibl B, Wobig H and Wolf G H, 1972 **Proceedings of the 7th Symposium on Fusion Technology, (Grenoble, France, 24-27 October 1972)**, (Commission of the European Communities, EUR 4938e) p 239

[20] Bykov V E, Georgievskij A V, Demchenko V V, Kuznetsov, Yu K, Litvinenko Yu A, Longinov A V, Pavlichenko O S, Rudakov V A, Stepanov K N and Tolok V T, 1990 **Fusion Technol. 17**, 140

[21] Beidler C D, 1989 **16th European Conf. on Controlled Fusion and Plasma Physics (Venice, Italy, 13-17 March 1989)** Vol. 13B (European Physical Society) Part II, p 675

[22] Mynick H E, 1983 **Phys. Fluids 26**, 1008

[23] Hastings D E, 1985 **Phys. Fluids 28**, 334

[24] Wakatani M, 1983 **Nucl. Fusion 23**, 817

[25] Dommaschk W, Lotz W and Nührenberg J, 1984 **Nucl. Fusion 24**, 794

[26] Shaing K C, Hirshman S P, Beasley C O Jr., Crume E C Jr. and van Rij W I, 1987 **Plasma Physics and Controlled Nuclear Fusion Research, Proc. 11th Int. Conf. (Kyoto, Japan, 1986)**, Vol. 2 (Vienna: IAEA) p 391

[27] Hitchon W N G and Mynick H E, 1987 **J. Plasma Physics 37**, 383

[28] Mynick H E, 1983 **Phys. Fluids 26**, 2609

[29] Kovrizhnykh L M, 1985 **Nucl. Fusion 25**, 1391

[30] Hitchon W N G, McLenithan K D and Mynick H E, 1983 **Nucl. Fusion 23**, 1143

[31] Galeev A A, Sagdeev R Z, Furth H P and Rosenbluth M N, 1969 **Phys. Rev. Lett. 22**, 511

[32] Mynick H E and Hitchon W N G, 1986 **Nucl. Fusion 26**, 425

[33] Beidler C D, 1990 **17th European Conf. on Controlled Fusion and Plasma Heating (Amsterdam, The Netherlands, 25-29 June 1990)** Vol. 14B (European Physical Society) Part II, p 513

[34] D'haeseleer W D, Hitchon W N G and Shohet J L, 1991 **J. Comput. Phys. 95**, 117

[35] Kovrizhnykh L M, 1969 **Sov. Phys. JETP 29**, 475

[36] Galeev A A and Sagdeev R Z, 1979 **Reviews of Plasma Physics, Vol. 7, Leontovich M A, Editor**, (Consultants Bureau, New York) p 257

[37] Beidler C D, Hitchon W N G and Shohet J L, 1987 **J. Comput. Phys. 72**, 220

[38] Shaing K C, Rome J A and Fowler R H, 1984 **Phys. Fluids 27**, 1

[39] Kovrizhnykh L M and Shasharina S G, 1990 **Nucl. Fusion 30**, 453